



Super-Lift Coefficient of Active Flow Control Airfoil: What is the Limit?

Yunchao Yang * Gecheng Zha †
 Dept. of Mechanical and Aerospace Engineering
 University of Miami, Coral Gables, Florida 33124
 E-mail: gzha@miami.edu

Abstract

This paper studies the enhancement of maximum lift coefficient and cruise efficiency using Co-Flow Jet (CFJ) active flow control airfoils. For potential flows, the maximum lift coefficient limit is derived as $C_{Lmax} = 2\pi(1+t/c)$ for any airfoil with thickness of t/c . The present study indicates that the CFJ active flow control airfoil is able to achieve the maximum lift coefficient that far exceeds the theoretical limit. It is named super-lift coefficient. The research is based on validated CFD simulation, which employs 2D RANS solver with Spalart-Allmaras(S-A) turbulence model, 5th order WENO scheme for the inviscid fluxes, and 4th order central differencing for the viscous terms. The momentum coefficient $C\mu$ studied is from 0.02 to 0.60 and the angle of attack (AoA) is from 0° to 74° .

Two CFJ airfoil configurations are created from the baseline NACA 6421 airfoil by translating the suction surface downward and adjusting the injection and suction slot sizes. One CFJ airfoil with smaller injection size is to achieve high C_{Lmax} for takeoff and landing. The other CFJ airfoil with larger injection size is to achieve high cruise efficiency. The maximum lift coefficient of 12.6 is achieved at AoA= 70° , M=0.063 and $C\mu = 0.60$. It is 66% higher than the theoretical limit of 7.6 for a 21% thickness airfoil with attached flow. The circulation achieved around the CFJ airfoil is so large that the stagnation point is detached from the airfoil solid body and the Kutta condition does not apply anymore.

The C_{Lmax} appears to have no limit. It depends on how much energy can be added to the flow, which varies with the active flow control method. This study indicates that the C_{Lmax} increase is very sensitive to energy addition when the C_{Lmax} is at low level. There is almost a linear relationship between the C_{Lmax} increase and the CFJ power consumed at low C_{Lmax} level. The C_{Lmax} eventually becomes plateaued even with continuously increased consumption of CFJ power. The C_{Lmax} correlates very well with the CFJ power coefficient.

For the super-lift condition at AoA of 70° , the vortex structures in the CFJ injection region appear to include 4 vortex layers one next to each other from the airfoil wall surface to the far field freestream : 1) clockwise boundary layer vortex sheet on the airfoil suction surface; 2) counter clockwise CFJ vortex layer due to the high momentum jet and the shear layer shed from the upstream leading edge boundary layer; 3) clockwise induced vortex layer induced by the high momentum co-flow jet via the mixing shear layer; and 4) the last vortex layer is a counter clockwise vortex layer, through which the secondary induced jet transits to the slower freestream velocity.

A new parameter named productivity efficiency defined as C_L^2/C_D is introduced to measure the cruise transportation capability of aircraft to carry a gross weight for maximum distance. For the second CFJ airfoil designed for cruise conditions with an assumed CFJ pumping efficiency of 80%, the peak aerodynamic efficiency $(L/D)_c$ that includes the CFJ power consumption is about 53% higher than that of the baseline airfoil. The productivity efficiency C_L^2/C_D of the CFJ airfoil is 109% higher.

The CFJ airfoil is demonstrated to be able to achieve super-lift coefficient for takeoff/landing at very high angle of attack and ultra-high efficiency for cruise at low angel of attack.

* Ph.D. Candidate, AIAA student member

† Professor, ASME Fellow, AIAA associate Fellow

Approved for public release; distribution is unlimited.

Nomenclature

<i>EBF</i>	External Blown Flaps
<i>IBF</i>	Internal Blown Flap
<i>CESTOL</i>	Cruise-Efficient Short Takeoff and Landing
<i>ESTOL</i>	Extreme Short Take-Off and Landing
<i>AoA</i>	Angle of Attack
<i>AFC</i>	Active Flow Control
<i>CFJ</i>	Co-Flow Jet
<i>FASIP</i>	Flow-Acoustics-Structure Interaction Package
<i>LE</i>	Leading Edge
<i>TE</i>	Trailing Edge
<i>RANS</i>	Reynolds-Averaged Navier-Stokes
<i>ZNMF</i>	Zero-Net Mass Flux
P	CFJ pumping power, $P = \frac{\dot{m}C_p T_{t2}}{\eta} (\Gamma^{\frac{\gamma-1}{\gamma}} - 1)$
η	CFJ pumping system efficiency, propeller efficiency
P_c	Power coefficient, $P_c = \frac{P}{\frac{1}{2}\rho_\infty V_\infty^3 S}$
PR	Total pressure ratio, Γ
C_L	Lift coefficient
C_D	Drag coefficient
C_M	Moment coefficient
C_μ	Jet momentum coefficient, $C_\mu = \frac{\dot{m}V_j}{\frac{1}{2}\rho_\infty V_\infty^2 S}$
C_{Lmax}	Maximum lift coefficient
$(L/D)_c$	Aerodynamic efficiency corrected for CFJ airfoil, $\frac{L}{D+P/V_\infty}$
C_{RW}	Aircraft Productivity parameter
C_L^2/C_D	Productivity efficiency coefficient
$(C_L^2/C_D)_c$	Productivity efficiency coefficient corrected for CFJ airfoil, $(C_L^2/C_D)_c = C_L^2/(C_D + P_c)$
R	Aircraft range
\bar{W}	Aircraft averaged weight during cruise
Re	Reynolds number
M	Mach number
M_{is}	Isentropic Mach number
C_p	Pressure coefficient
c_p	Constant pressure specific heat
γ	Air specific heats ratio
S	Planform area of the wing
ρ_∞	Freestream density
V_∞	Freestream velocity
T_t	Total temperature
P_t	Total pressure
H_t	Total enthalpy
α	Angle of attack
\dot{m}	Mass flow
C	Chord length
j	Subscript, stands for jet
c	Subscript, stands for corrected

1 Introduction

Maximum lift coefficient, C_{Lmax} , of an airfoil is a very important issue in aerodynamics theory and in engineering practice. In aerodynamics theory, Smith's[1] pioneering research in 1975 gives a limit below:

$$C_{Lmax} = 2\pi(1 + \frac{t}{c}) \quad (1)$$

which is based on inviscid potential flow model at an angle of attack(AoA) of 90° . Since it is potential flow with no boundary layer, the flow is treated that it will never get stalled. For a cylinder, since t is equal to c , the theoretical C_{Lmax} limit will be $4\pi=12.57$. For the NACA 6421 airfoil studied in this paper, the theoretical limit C_{Lmax} will be 7.6. The derivation of the maximum lift coefficient for potential flow is provided in Appendix I.

In practice, C_{Lmax} is extremely important to determine the takeoff/landing distance and noise. The higher the C_{Lmax} , the shorter the takeoff/landing distance, and the lower the airframe noise. Achieving high C_{Lmax} is hence critical to increase future airport capacity and reduce airport community noise. This is particular true with the world economic growth that enables more people travel by air. According to FAA(2007), there are 22 major US airports that are predicted to suffer from capacity shortage for the next two decades. The extremely short takeoff/landing(ESTOL)[2, 3] and the Cruise-Efficient Short Takeoff and Landing (CESTOL) concepts[4] are strongly advocated to be introduced for future U.S. National Airspace System (NAS) civil aviation environment.

Smith's theory [1] provides the theoretical foundation for the multi-element flap high lift system. The more airfoil elements are used, the more the lifting surface meanline can approach a half circle. By observing the trend of the C_{Lmax} growing from 2 in 1935 to 3 in 1965, Smith[1] asked then "By 1995 will we have advanced to 4?". He did show a 7-element flap system that achieves a C_{Lmax} close to 4. However, flap high lift system is very complicated and expensive to make [5]. The airliner manufacturers are moving toward simpler high lift systems with less airfoil elements instead of the other way around [5]. Hence the answer to Smith's question is that today's high lift system and C_{Lmax} level is not much different from those 5 decades ago in 1965.

Aircraft design needs to consider the whole flight envelop including takeoff/landing and cruise. The C_{Lmax} matters for takeoff/landing, efficiency matters for the cruise to maximize range, pay load, and fuel consumption reduction. The ratio of lift to drag, or C_L/C_D , is usually used to represent the aircraft aerodynamic efficiency. In this paper, we introduce a productivity efficiency, C_L^2/C_D , to represent the aircraft cruise capability to move a gross weight by its maximum distance.

1.1 What is the C_{Lmax} Limit?

The numerical simulation conducted in this research achieves airfoil C_{Lmax} far greater than that defined by Eq. (1) using active flow control. We were puzzled by the results and were not fully sure if it is physically sound.

By surveying the literature, it is found that one of the earliest study to explore C_{Lmax} was done by Prandtl for his famous experiment to enhance lift by rotating the cylinder in a flow [6]. A spinning cylinder transfers its mechanical energy to the flow via viscosity with no-slip wall boundary condition. He argued that the maximum lift generated by a spinning cylinder in a uniform flow is limited to 4π (≈ 12.57), which is consistent with the C_{Lmax} defined by Eq. (1) [7].

Tokumar and Dimotakis (1993)[8] studied the mean lift acting on a rotating cylinder in a uniform flow. It is devised based on an inviscid point-vortex model. Their results for $Re = 3.8 \times 10^3$ show that Prandtl's limit on lift coefficient ($C_{Lmax} = 4\pi$) can be exceeded, as shown in Fig. 1. They suggested that perhaps it is the unsteady effects that weaken Prandtl's hypothesis. And the three dimensional effects are responsible for the increase of the lift coefficient compared to a purely two-dimensional flow. Their results indicate that the faster the cylinder spins, the higher lift coefficient it can achieve, but the relation is not linear. Initially, the flow responds sensitively to the spinning speed of the cylinder with the lift coefficient increased about linearly with the spinning speed. However, when the cylinder spins too fast, the flow is not able to absorb more energy from the rotating cylinder and the lift increase becomes plateaued (see Fig. 1).

Another experiment on the circular cylinder lifting surface was conducted by Lockwood et al. (1960) [9] in NASA Langley to provide lift on takeoff and landing by blowing on the circular fuselage of a hypersonic aircraft. As shown in Fig. 2, the maximum lift coefficient over $C_L \approx 20$ is measured at high $C_\mu \approx 5$ for a very low Reynolds number flow over an end-plated-cylinder with multiple injection slots [9], [10].

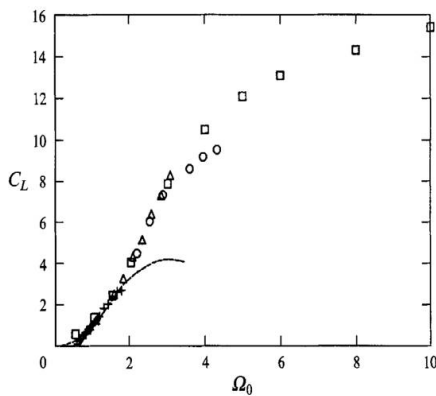


Figure 1: Lift coefficient C_L vs cylinder rotating speed in the rotating cylinder experiment. (Plot is adopted from [8])

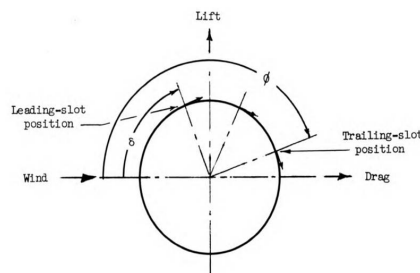
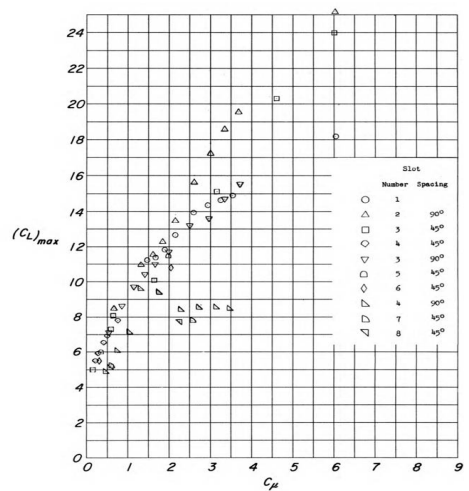


Figure 2: Lifting cylinder using tangential blowing from surface slots. (Plot is adopted from [9])



Above cylinder lift enhancement experiments indicate that the C_{Lmax} defined by Eq. (1) has been exceeded by adding energy to the flow using active flow control, such as rotating cylinder or jet injection. The C_{Lmax} limit from the potential flow is the result of imposing Kutta condition, which is necessary for potential flow, but not a true physical condition that realistic flows must satisfy.

Then the next question is “What is the limit?”. The answer appears to be that there is no limit for C_{Lmax} . It depends on how much energy can be added to the flow. Depending on the active flow control method, the flow will not be able to absorb more energy at certain point, at which the C_{Lmax} will reach the limit. The present research supports this statement. So far, the lift coefficient breaking the theoretical limit is only seen for cylinder flows. No airfoil is shown to have such capability until the present study.

1.2 ESTOL Performance with Flow Control

The only large transport with ESTOL performance is the US military transport C-17 as shown in Fig. 3, which has a short takeoff/landing distance of 3000ft using the external blown flaps (EBF) flow control technology

developed in mid-50s by NASA. As displayed in Fig. 3, EBF augments lift coefficient by directing the engine exhaust jets below the wings to flow through the highly deflected multi-element flap systems.

The aerodynamics principle of EBF is that the engine jets energize the wing suction surface boundary layer through the slots of the flap system and keep the flow attached with the highly cambered airfoil formed by the multi-element flaps. The EBF comes with a price of significantly increased drag. In addition, the heavy and costly titanium alloy must be used for the wing structure to resist the high temperature of the engine jets. For military transports, the engines hung beneath the wings for EBF also have the disadvantages of large radar cross sections.

The other possible lift enhancement technology using flow control is the internally blown flap (IBF), which introduces mass flow from the compressor (bleed) of the engine and blow the air on the suction surface leading edge (LE) and trailing edge (TE) of the wing. IBF augments lift based on the circulation control (CC) airfoil concept due to Coanda effect, which exists at the airfoil leading edge due to the LE suction and in the vicinity of a blunt trailing edge based on its low base pressure. Hence, a blunt TE is required to render the CC effective. However, a thick TE increases drag at cruise condition. To overcome the dependence on a blunt TE, a movable flap at the airfoil TE must be used [11]. But moving parts impose a weight penalty.

One considerable penalty of CC airfoil blowing is the dumped mass flow induced from the propulsion system bleed or other pumping systems. The mass flow rate of the engine bleed is directly proportional to the reduction of the thrust, i.e. the engine will suffer 1-2% thrust reduction for 1% blow rate used for wing flow control, and suffer 1-3% fuel consumption increase depending on whether the bleed is from the compressor front stage or back stage. Furthermore, a CC airfoil must include an extra drag, “equivalent” drag [12, 13] in addition to the measured drag in a wind tunnel. This is because a flow mass withdrawn from freestream is needed to supply the injection mass (mass conservation law). The withdraw of freestream mass flow will generate a ram drag, which can not be avoided, but is not measured in wind tunnel testing.



Figure 3: C-17 military transport with STOL performance.



Figure 4: The Double-Bubble future aircraft concept by MIT



Figure 5: The concept aircraft SAX-40

Future military and commercial transports are more and more evolved toward highly integrated airframe-propulsion system such as the “double-bubble”[14] and SAX[15] shown in Fig. 4 and 5. A simple flapless high lift system without relying on engines is desirable.

The recent concept of co-flow jet (CFJ) flow control airfoil, developed by Zha et al. [12, 16, 17, 18, 19, 20, 21, 22, 23, 24] shows a great potential to fulfill the role of future flapless high lift system. The CFJ airfoil achieves a dramatically lift augmentation, drag reduction and stall margin increase at low energy expenditure. It can not only achieve ESTOL performance with ultra-high maximum lift coefficient, but also significantly enhance cruise efficiency and cruise lift coefficient (wing loading) from subsonic to transonic conditions [22, 23, 24]. The CFJ airfoil has great potential to radically change the overall aircraft design philosophy from subsonic to transonic speeds.

1.3 The Co-Flow Jet Airfoil

The CFJ airfoil has an injection slot near the LE and a suction slot near the TE on the airfoil suction surface as sketched in Fig. 6. A small amount of mass flow is withdrawn into the airfoil near the TE, pressurized and energized by a pumping system inside the airfoil, and then injected near the LE in the direction tangent to the main flow. The whole process does not add any mass flow to the system and hence is a zero-net mass-flux (ZNMF) flow control. It is a self-contained high lift system with no moving parts.

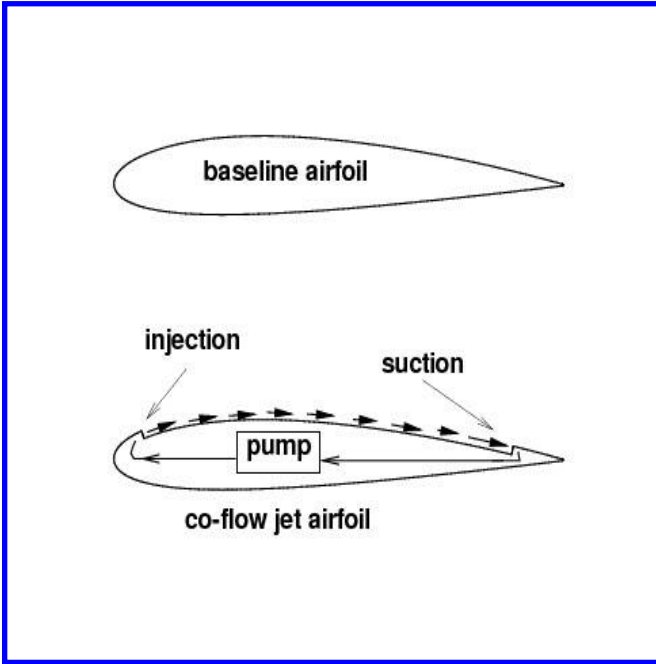


Figure 6: Baseline airfoil and CFJ airfoil.

The fundamental mechanism of the CFJ airfoil is that the turbulent mixing between the jet and main flow energizes the wall boundary-layer, which dramatically increases the circulation, augmenting lift, and reducing the total drag(or generates thrust) by filling the wake velocity deficit. The CFJ airfoil has a unique low energy expenditure mechanism because the jet gets injected at the leading edge suction peak location, where the main flow pressure is the lowest and makes it easy to eject the flow, and it gets sucked at near the trailing edge, where the main flow pressure is the highest and makes it easy to withdraw the flow.

Fig. 7 adopted from [23] is the PIV measured velocity field of the CFJ-NACA-6415 airfoil at the AoA of 25° and C_μ of 0.06, which has the flow attached and a higher speed within the wake than in the freestream. In this case, thrust is generated. The baseline NACA-6415 airfoil has massive flow separation at this AoA. Fig. 8 shows the wind tunnel test results of several CFJ airfoils at Mach number of 0.1. The CFJ airfoil achieves a C_{Lmax} of about 5, more than 3 times higher than the baseline airfoil. It also obtains an enormous thrust coefficient of about 0.8. A CFJ wing is hence can be used as a distributed thrust system.

Fig. 9 from [23] shows the computed power coefficient compared with the experiment. The power coefficient decreases with the increase of AoA up to 15° and then rises at higher AoA. It is because when the AoA is increased and the flow still remains attached, the airfoil LE suction effect becomes stronger with lower static pressure in

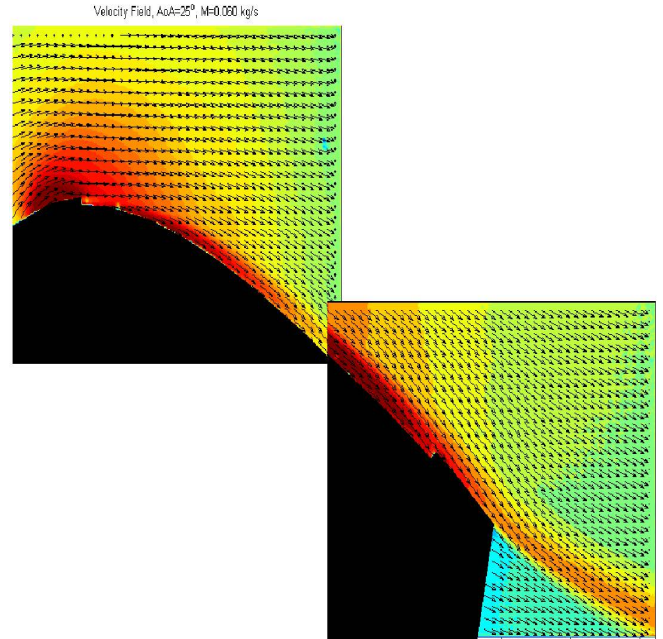


Figure 7: Attached flow of CFJ NACA 6415 airfoil at AoA= 25° measured by PIV in experiment, C_μ of 0.06, $M=0.1$ (Plot adopted from [23]).

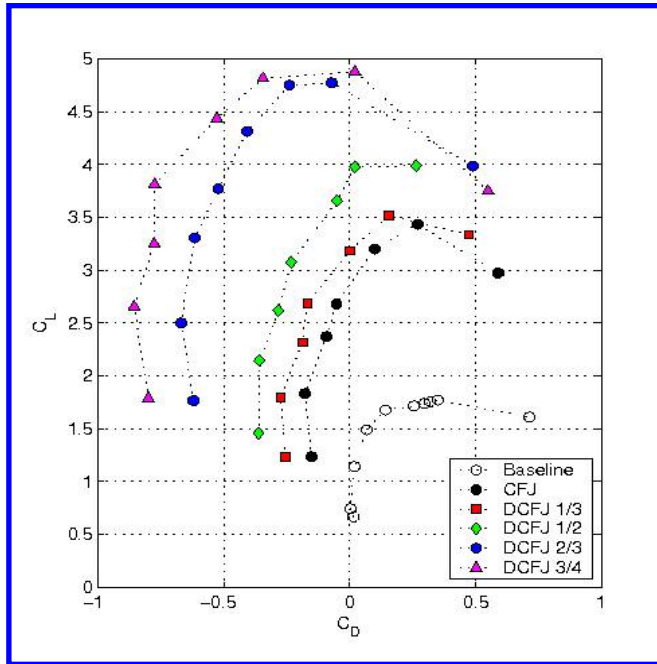


Figure 8: Measured drag polars of discrete CFJ airfoils with different obstruction factors at mass flow $\dot{m} = 0.06 \text{ kg/s}$ (Plot adopted from [23]).

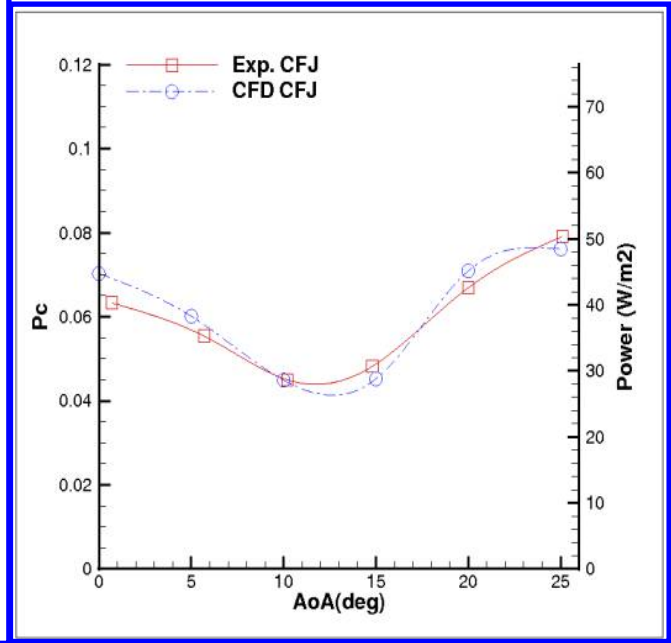


Figure 9: Computed power coefficient compared with experiment at $M=0.03$ and $C_\mu = 0.08$ (Plot adopted from [23]).

the region of the injection jet, and hence less power is needed to generate the jet with the same momentum coefficient. However, when the AoA is beyond the separation value, the boundary layer is deteriorated with large energy loss and the suction power is significantly increased. More information on CFJ airfoil can be found in [12, 16, 17, 18, 19, 20, 21, 23, 22, 24, 25]

1.4 Objective

The objective of this paper is two folds: 1) to explore the maximum lift coefficient capability of the CFJ airfoil. It is our interest to see if this promising active flow control concept can break the theoretical inviscid limit. It is also our interest to study the C_{Lmax} relationship with the energy expenditure. 2) To demonstrate that the CFJ airfoil can also achieve high cruise lift coefficient and high efficiency when the flow is benign at low AoA.

2 CFJ Parameters

This section gives the important parameters to evaluate a CFJ airfoil performance.

2.1 Lift and Drag Calculation

The momentum and pressure at the injection and suction slots produce a reactionary force, which is automatically measured by the force balance in wind tunnel testing. However, for CFD simulation, the full reactionary

force needs to be included. Using control volume analysis, the reactionary force can be calculated using the flow parameters at the injection and suction slot opening surfaces. Zha et al. [12] give the following formulations to calculate the lift and drag due to the jet reactionary force for a CFD simulation. By considering the effects of injection and suction jets on the CFJ airfoil, the expressions for these reactionary forces are given as :

$$F_{x_{cfj}} = (\dot{m}_j V_{j1} + p_{j1} A_{j1}) * \cos(\theta_1 - \alpha) - (\dot{m}_j V_{j2} + p_{j2} A_{j2}) * \cos(\theta_2 + \alpha) \quad (2)$$

$$F_{y_{cfj}} = (\dot{m}_{j1} V_{j1} + p_{j1} A_{j1}) * \sin(\theta_1 - \alpha) + (\dot{m}_{j2} V_{j2} + p_{j2} A_{j2}) * \sin(\theta_2 + \alpha) \quad (3)$$

where the subscripts 1 and 2 stand for the injection and suction respectively, and θ_1 and θ_2 are the angles between the injection and suction slot surfaces and a line normal to the airfoil chord. α is the angle of attack.

The total lift and drag on the airfoil can then be expressed as:

$$D = R'_x - F_{x_{cfj}} \quad (4)$$

$$L = R'_y - F_{y_{cfj}} \quad (5)$$

where R'_x and R'_y are the surface integral of pressure and shear stress in x (drag) and y (lift) direction excluding the internal ducts of injection and suction. For the CFD simulation, the total lift and drag are calculated using Eqs. (4) and (5).

2.2 Jet Momentum Coefficient

The jet momentum coefficient C_μ is a parameter used to quantify the injection intensity. It is defined as :

$$C_\mu = \frac{\dot{m} V_j}{\frac{1}{2} \rho_\infty V_\infty^2 S} \quad (6)$$

where \dot{m} is the injection mass flow, V_j the injection velocity, ρ_∞ and V_∞ denote the free stream density and velocity, and S is the platform area.

2.3 Power Coefficient

The CFJ can be implemented by mounting a pumping system inside the wing that withdraws air from the suction slot and blows it into the injection slot. The power consumption can be determined by the jet mass flow and total enthalpy change as the following :

$$P = \dot{m}(H_{t1} - H_{t2}) \quad (7)$$

where H_{t1} and H_{t2} are the total enthalpy in the injection cavity and suction cavity respectively, P is the Power required by the pump and \dot{m} the jet mass flow rate. Introducing the pumping efficiency η and total pressure ratio of the pump $\Gamma = \frac{P_{t1}}{P_{t2}}$, the power consumption can be expressed as :

$$P = \frac{\dot{m} C_p T_{t2}}{\eta} (\Gamma^{\frac{\gamma-1}{\gamma}} - 1) \quad (8)$$

The power consumption can be expressed as a power coefficient below:

$$P_c = \frac{P}{\frac{1}{2}\rho_\infty V_\infty^3 S} \quad (9)$$

In this research, the pumping efficiency of 100% is used for all the simulations unless indicated otherwise.

2.4 Corrected Aerodynamic Efficiency

The conventional airfoil aerodynamic efficiency is defined as $\frac{L}{D}$. However since CFJ active flow control consumes energy, the CFJ corrected aerodynamic efficiency is modified to take into account the energy consumption of the pump. The formulation of the corrected aerodynamic efficiency for CFJ airfoils is :

$$\left(\frac{L}{D}\right)_c = \frac{L}{D + \frac{P}{V_\infty}} = \frac{C_L}{C_D + P_C} \quad (10)$$

where V_∞ is the free stream velocity, P is the CFJ pumping power, and L and D are the lift and drag generated by the CFJ airfoil. This formulation converts the power consumed by the CFJ into the drag of the airfoil. If the pumping power is set to 0, this formulation returns to the aerodynamic efficiency of a conventional airfoil.

3 Aircraft Productivity

The transportation ability of an airplane is measured by how much total weight the aircraft can move for the maximum distance. We use a term ‘‘productivity’’ defined as the product of the total weight by the maximum range to represent the transportation ability of an airplane.

For a jet engine airplane, the total weight of the aircraft decreases during flight. A non-dimensional productivity parameter is hence defined using the aircraft averaged weight as below:

$$C_{RW} = \frac{R\bar{W}}{\frac{1}{2c_t}\bar{\rho}V_\infty^3 S} = \frac{C_L^2}{C_D} \ln \frac{W_0}{W_f} \quad (11)$$

where R is the aircraft range, \bar{W} is the averaged weight of the aircraft during cruise, c_t is the engine cruise thrust specific fuel consumption[fuel weight(N)/(thrust(N) s)], $\bar{\rho}$ is the averaged air density during cruise due to altitude variation, S is the wing platform area, W_0 is the aircraft initial gross weight at takeoff, W_f is the final weight at landing. This formulation is obtained from the Breguet Range Equation. The productivity parameter represents the productivity of the aircraft with the fuel consumed per unit time.

For a propeller engine airplane, the productivity parameter is defined as:

$$C_{RW} = \frac{R\bar{W}}{\frac{1}{2c}\bar{\rho}V_\infty^2 S} = \eta \frac{C_L^2}{C_D} \ln \frac{W_0}{W_f} \quad (12)$$

where c is the fuel specific consumption of the propeller engine[fuel weight(N)/(BHP(W) s)], η is the propeller efficiency.

For a full electric battery powered propeller airplane, the aircraft weight will not change during flight. The productivity parameter is defined as:

$$C_{RW} = \frac{RW}{\frac{1}{2c}\rho V_\infty^2 S E_c/g} = \eta \frac{C_L^2 W_b}{C_D W_0} \quad (13)$$

where E_c is the battery specific energy density (Wh/kg), W_b is the total battery weight.

To compare aircraft that have the same ratio of initial weight to final weight with the same engine fuel consumption or battery energy density, the only factor affecting their productivity parameter is C_L^2/C_D . We hence name C_L^2/C_D as productivity efficiency.

We consider the productivity efficiency $C_L^2/C_D = C_L(C_L/C_D)$ as a more comprehensive parameter than the conventional aerodynamic efficiency C_L/C_D to measure the merit of an airplane aerodynamic design for cruise performance. The former includes not only the information of C_L/C_D , but also the information of the aircraft weight C_L . For example, for two airplane designs having the same C_L/C_D with one C_L twice larger than the other, if the wing sizes are the same, one airplane will be able to carry twice more weight than the other with productivity and wing loading increased by 100%. Such a large difference is not reflected by C_L/C_D , but very well reflected by C_L^2/C_D .

The definition of C_L/C_D in general is a suitable measure of merit for conventional aircraft design. This is because at a certain Mach number regime, the maximum C_L/C_D is usually achieved at low angle of attack within the drag bucket and is more or less the same for different airfoil designs. In other words, for the same optimum C_L/C_D , the C_L is about the same. A typical C_L for subsonic airfoil is about 0.4 and for transonic airfoil is about 0.7.

For CFJ airfoil, the minimum CFJ pumping power occurs at a fairly high AoA as shown in Fig. 9 [21, 23]. With the augmentation of CFJ, the subsonic cruise lift coefficient of a CFJ airfoil is typically 2 to 3 times higher than the conventional airfoil with about the same $(C_L/C_D)_c$ [25]. Such a high lift coefficient is unattainable for conventional airfoil since they would be either stalled or near stalled with very high drag. Hence for CFJ aircraft design, the productivity efficiency $C_L^2/C_D = C_L(C_L/C_D)$ is more informative to be used to reflect the aerodynamic performance. The corrected productivity efficiency for CFJ airfoils is $(C_L^2/C_D)_c = C_L^2/(C_D + P_c)$.

4 CFD Simulation Setup

4.1 CFD Code

The in-house FASIP (Flow-Acoustics-Structure Interaction Package) CFD code is used to conduct the numerical simulation. The 2D Reynolds averaged Navier-Stokes (RANS) equations with one-equation Spalart-Allmaras [26] turbulence model is used. A 5th order WENO scheme for the inviscid flux [27, 28, 29, 30, 31, 32] and a 4th order central differencing for the viscous terms [27, 31] are employed to discretize the Navier-Stokes equations. The low diffusion E-CUSP scheme used as the approximate Riemann solver suggested by Zha et al [28] is utilized with the WENO scheme to evaluate the inviscid fluxes. Implicit time marching method using Gauss-Seidel line relaxation is used to achieve a fast convergence rate [33]. Parallel computing is implemented to save wall clock simulation time [34]. The RANS solver is validated for CFJ airfoil simulations [19, 23, 24, 25, 35, 36].

4.2 Boundary Conditions

The 3rd order accuracy no slip condition is enforced on the solid surface with the wall treatment suggested in [37] to achieve the flux conservation on the wall. Total pressure, total temperature and flow angles are specified as the inlet boundary conditions for the upstream portion of the farfield boundary and inside the injection cavity. Constant static pressure is used for the downstream farfield boundary and inside the suction cavity.

4.3 C_μ Iteration:

To achieve zero net mass flux with the CFJ flow control, the mass flow exiting the injection slot must be equal to the mass flow entering the suction slot, i.e. $\dot{m}_{inj} = \dot{m}_{suc}$. The prescribed jet momentum coefficient C_μ is achieved by adjusting the injection cavity total pressure. Total temperature is assumed constant during this process. The injection and suction mass flow rates are matched by adjusting the suction cavity static pressure. The iterative process is conducted throughout the simulation until the specified momentum coefficient is reached and the injection and suction mass flow match within the acceptable tolerance, which is 0.2% for the present study..

4.4 Mesh

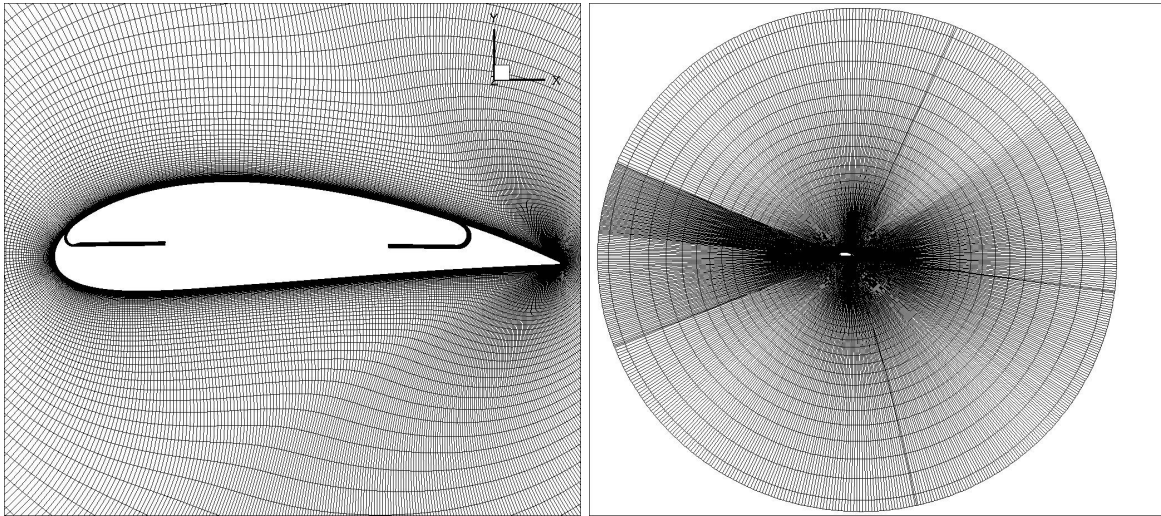


Figure 10: Computational mesh for CFJ calculation ($\text{AoA} = 5^\circ$)

The 2D structured meshes are constructed using the O-mesh topology in order to achieve high mesh quality within the airfoil boundary. A total of 1201 points are placed around airfoil, 601 points on suction surface, 601 points on the pressure surface and 151 points normal to the airfoil with an additional 41 points across the jet. The total mesh size is 205,600 cells, and is partitioned into 8 blocks for parallel computation. The farfield boundary is located 15 chords away from the airfoil. To resolve the turbulent boundary layer, the first grid point is placed at $y^+ \approx 1$. The block definition is found in Table 1 and the mesh topology is shown in Fig. 10.

A mesh refinement study was performed for the baseline NACA6421 and CFJ6421 airfoil at $M=0.063$ and $\text{Re}=3,030,000$ by adjusting the mesh size in the chord-wise and wall-normal direction, as shown in Table 2 and 3.

Table 1: Mesh for CFJ 6421 airfoil calculation

Block	ξ -Direction	η -Direction	Cell number	location
1-5	241	151	36000	around the airfoil
6	201	41	8000	Injection block
7	241	41	9600	Connection
8	201	41	8000	Suction block
Total mesh size			205600	

The mesh size of 601x151 is used for the baseline airfoil study. For the CFJ airfoil, the mesh size of 1201x151 is adopted. The C_L, C_D, C_M results are converged based on mesh size as shown in Table 2 and 3.

Table 2: Mesh independence study for the baseline NACA6421 airfoil at AoA=5°

Case	AoA	Grid size	C_L	C_D	C_M
1	5	601 × 151	1.011	0.020	-0.102
2	5	601 × 301	1.006	0.020	-0.100
3	5	1201 × 151	1.006	0.021	-0.103

Table 3: Mesh independence study for the CFJ6421 SST016-SUC053-INJ009 airfoil at AoA=70° and $C_\mu = 0.25$

Case	AoA	Grid size	C_L	C_D	C_M
1	5	601 × 151	8.873	0.065	-0.547
2	5	1201 × 151	8.275	0.314	-0.510
3	5	1201 × 301	8.222	0.324	-0.508
4	5	2401 × 151	8.249	0.327	-0.512

5 Results and Discussion

The CFJ airfoil configurations are created from the baseline NACA 6421 airfoil by translating the suction surface downward, which is defined as the suction surface translation (SST). The CFJ injection and suction slot sizes are iterated with trade study to obtain high lift coefficient for take-off and landing, and high aerodynamic efficiency for cruise condition. Fig. 11 shows several CFJ airfoil geometries with various SST, injection slot sizes and suction slot sizes in the trade study.

The CFJ airfoils are designed differently to achieve the max lift coefficient for takeoff/landing and to achieve maximum efficiency at cruise. In general, to have high C_{Lmax} , it is more effective to have smaller injection size with higher injection velocity, which will give higher injection jet momentum and lower mass flow rate if the C_μ is fixed. However, the power coefficient of the CFJ airfoil is also high with smaller injection size because the jet suffers high energy loss going through small holes. Thus for the cruise condition that a high efficiency is more important, a larger injection slot size with lower jet velocity and loss is more desirable. The results below are therefore presented in two separated sections, one for maximum lift coefficient at takeoff/landing with very high AoA and the other one for high efficiency at cruise condition with low AoA.

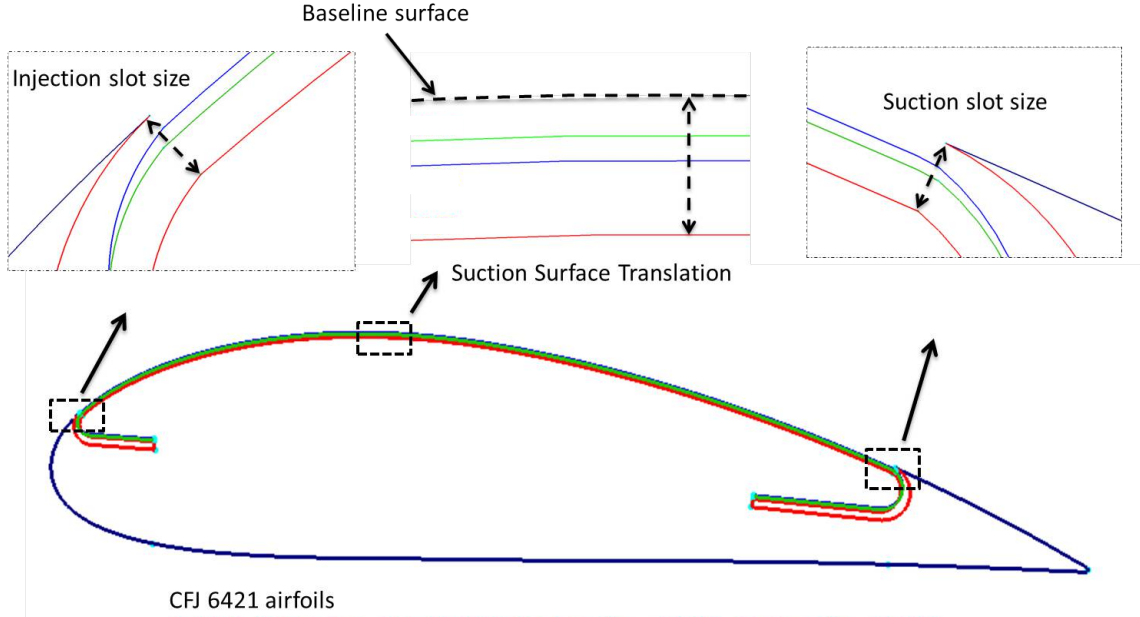


Figure 11: CFJ6421 airfoil geometry

Table 4: CFJ6421 airfoil geometry parameters for takeoff/landing and cruise condition

Case	CFJ6421 airfoil	SST (%C)	INJ slot size (%C)	SUC slot size (%C)
Takeoff/Landing	SST016-SUC053-INJ009	0.16	0.09	0.53
Cruise	SST143-SUC133-INJ065	1.43	0.65	1.33

Table 4 gives the detailed parameters of the two CFJ airfoils designed for takeoff/landing and cruise condition, including the injection and suction slot size normalized by chord length(C), and the injection jet momentum coefficient used. The 3-digit number in the naming convention stands for the SST distance, injection slot size, and suction slot size normalized by the airfoil chord.

5.1 Maximum Lift Coefficient

This section is to investigate the maximum lift coefficient for the CFJ airfoil CFJ6421-SST016-SUC053-INJ009, which has a thin injection slot size of $0.09\%C$, suction slot size of $0.53\%C$, and the suction surface translation (SST) of $1.6\%C$. A comprehensive parametric study was conducted to obtain this CFJ airfoil geometry, which will be presented in another paper.

5.1.1 Airfoil Characteristics

For the low speed takeoff/landing simulation, the Mach number of 0.063 and Reynolds number of 3.03 million are used. The jet momentum coefficients $C_{\mu} = 0.04, 0.15$, and 0.25 are simulated for the initial simulation to

obtain the whole characteristics. The simulated AoAs vary from 0° to 74° with an increment of 4° . As the lift and drag coefficient shown in Fig. 12 and 13, the CFJ airfoil flow remains attached at AoA of 70° . To explore the maximum lift coefficient, higher momentum coefficient of 0.35, 0.4, 0.5 and 0.6 are simulated only at AoA of 70° as presented in the results.

Table 5: Takeoff/Landing simulation parameters

CFJ6421 airfoil	Mach number	Reynolds number	AoA	C_μ
SST016-SUC053-INJ009	0.063	3,030,000	2° - 74°	0.04,0.15,0.25, 0.35,0.40,0.50,0.60

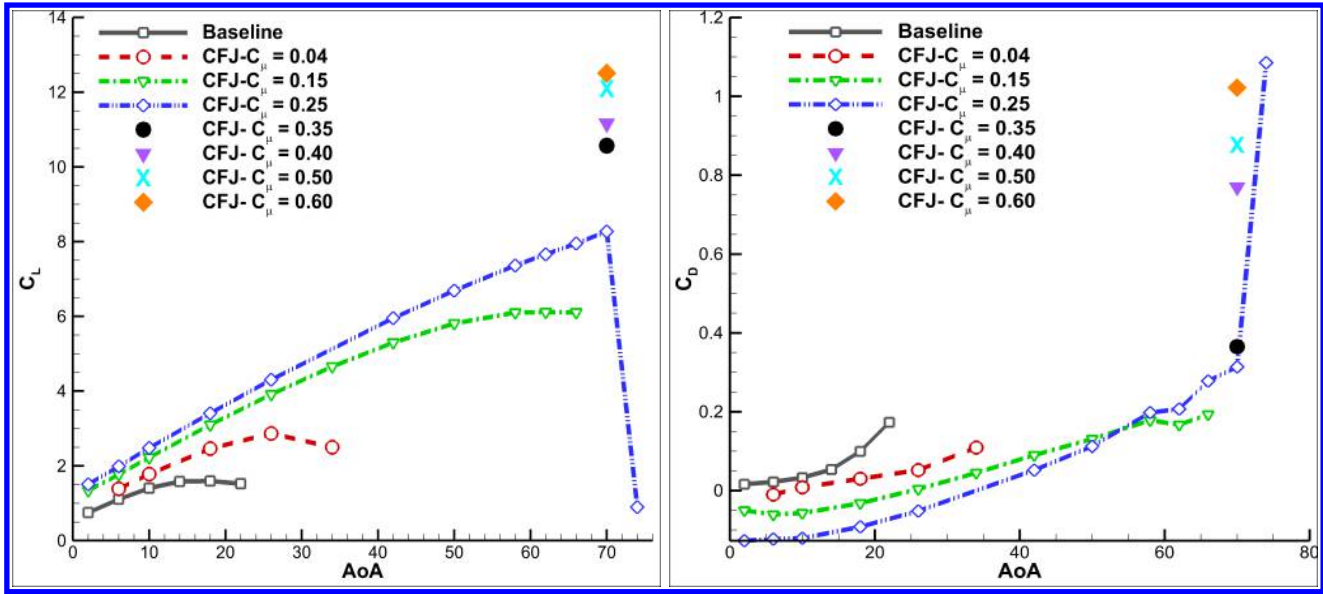


Figure 12: Lift and Drag coefficient vs AoA for the baseline and CFJ6421-SST016-SUC053-INJ009 airfoil.

Fig. 12 shows the computed lift and drag coefficients at different momentum coefficients. The baseline NACA6421 airfoil is stalled at $\text{AoA}=18^\circ$ with the maximum lift coefficient of 1.42. The maximum lift coefficients for the CFJ airfoils are increased dramatically to 8.3 at $C_\mu = 0.25$ and the stall AoA is increased to $\text{AoA}=70^\circ$. At AoA of 70° , the maximum lift coefficient continues to rise with increasing C_μ and reaches a value of 12.60 at $C_\mu=0.60$. This value is far greater than the C_{Lmax} of 7.6 defined for this airfoil based on Eq. (1). It also exceeds the maximum lift coefficient of 4π for all lifting devices based on the potential flow theory as indicated by Eq. (1). The lift coefficient greater than the maximum lift coefficient limit defined by potential flow is named as “Super-Lift Coefficient”.

The drag coefficients of the CFJ airfoil are all reduced compared with that of the baseline NACA6421 airfoil. The negative drag coefficient is the thrust created by the CFJ. As the AoA increases, the drag coefficient is increased slowly until the flow is stalled when a massive flow separation occurs. At high momentum coefficient of $C_\mu > 0.25$ at high angle of attack such as $\text{AoA}=70^\circ$, the ultra high lift also generates very high pressure drag as shown in Fig. 12.

For the pure aerodynamic ratio of L/D in Fig. 13, CFJ airfoil has extraordinarily high values because the drag can be so small or negative. The pure L/D will be used for a CFJ aircraft to decide its weight and propulsion systems. The negative drag will create negative L/D , which is a feature that the CFJ airfoil can be used as

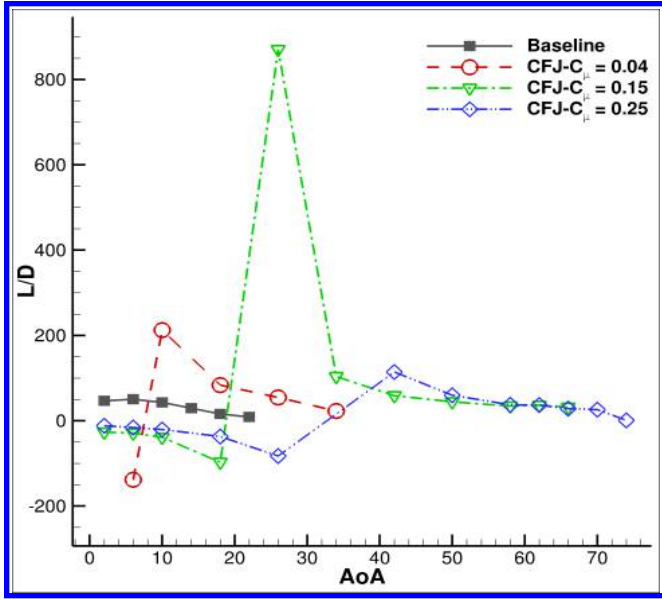


Figure 13: Aerodynamics efficiency L/D vs AoA for the baseline and CFJ6421-SST016-SUC053-INJ009 airfoil.

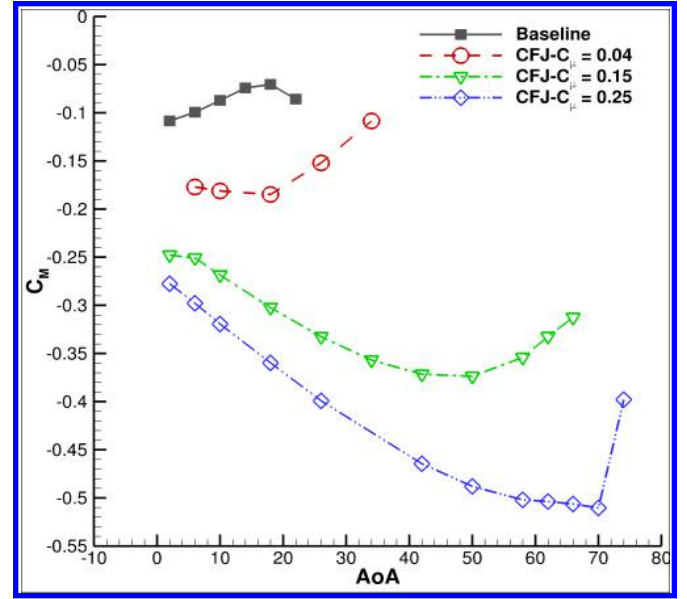


Figure 14: Moment coefficient C_M vs AoA for the baseline and CFJ6421-SST016-SUC053-INJ009 airfoil.

distributed thrust source. As shown in Fig. 13 for the C_μ from 0.04 to 0.25, the L/D are negative up to AoA about 30° . That means the CFJ airfoil will propel itself without a propulsion system. Even when the AoA is near 70° with C_L about 8, the L/D is at a high level of about 50. This means that the aircraft does not need a large engine and the system can be more optimized to favor cruise efficiency.

The pitching moment coefficient about the 1/4 chord point is shown in Fig. 14. The nose down moment coefficient C_M is significantly increased with the high C_μ and very high lift coefficient. For small injection momentum coefficient $C_\mu = 0.04$, the nose down moment coefficient is increased moderately. The high nose down moment may be better compensated by using canard as pitching moment control surface.

The corrected aerodynamic efficiency $(L/D)_c$ is plotted in Fig. 15. For the baseline airfoil, $(L/D)_c = (L/D)$ and the maximum $(L/D)_c$ of 50 occurs at AoA= 6° . The maximum $(L/D)_c$ of 25 is obtained for this CFJ airfoil at AoA= 22° and $C_\mu = 0.04$. Since this CFJ airfoil is designed to achieve high maximum lift coefficient at takeoff/landing, not for high cruise efficiency, it is expected that the maximum $(L/D)_c$ is substantially lower than that of the baseline airfoil.

The productivity efficiency coefficient $(C_L^2/C_D)_c$ is given in Fig. 16. The baseline maximum $(C_L^2/C_D)_c$ is 60 at AoA= 10° . For the CFJ airfoil, the maximum $(C_L^2/C_D)_c = 70$ is obtained at AoA= 26° and $C_\mu = 0.04$. Even though this airfoil is not designed for cruise efficiency, the maximum productivity efficiency is still better than the baseline airfoil due to its higher lift coefficient.

The power coefficients of the CFJ pumping are calculated based on Eq. (8) and (9) using a constant efficiency value of 100%. The results are shown in Fig. 17. The power coefficient decreases with the increase of AoA until the airfoil is stalled. Fig. 18 is the total pressure ratio PR . The pumping power is largely determined by the total pressure ratio PR between the injection and suction cavity. The total pressure ratio PR has a similar pattern to the power coefficient, which decreases with the increasing AoA until the airfoil is stalled. This is a typical behavior of CFJ airfoil [23], because when the AoA is increased, the static pressure of the main flow at the injection region is decreased. The required injection total pressure is hence decreased accordingly to achieve the same C_μ . The

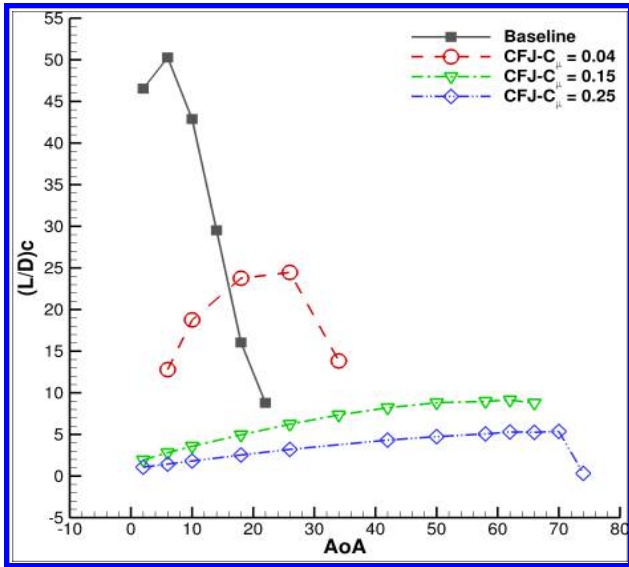


Figure 15: Corrected aerodynamic efficiency $(L/D)_c$ vs AoA for the baseline and CFJ6421-SST016-SUC053-INJ009 airfoil.

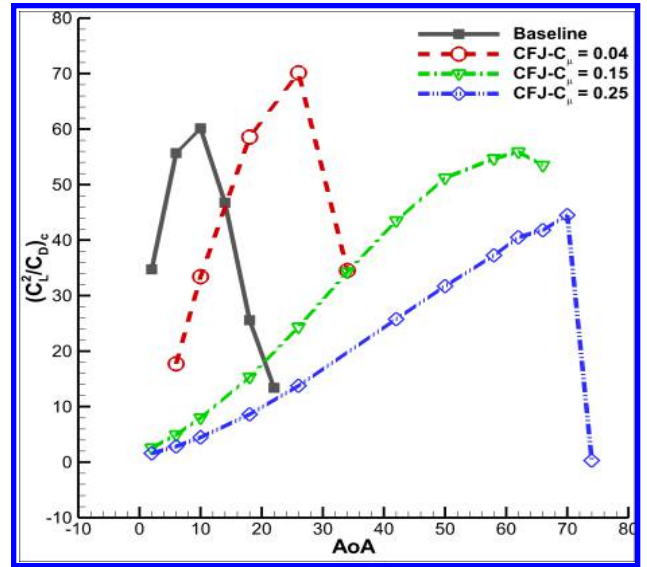


Figure 16: Corrected productivity efficiency $(C_L^2/C_D)_c$ vs AoA for the baseline and CFJ6421-SST016-SUC053-INJ009 airfoil.

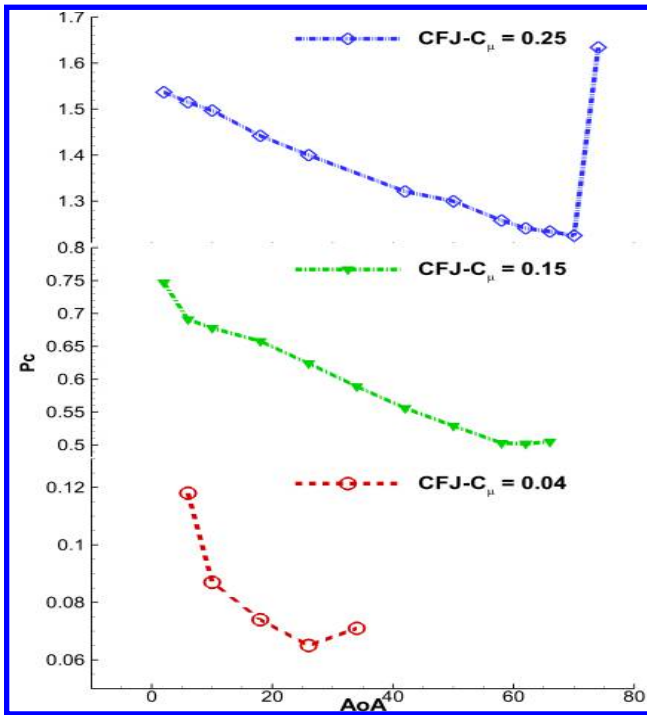


Figure 17: Power coefficient P_c for the CFJ6421-SST016-SUC053-INJ009 airfoil.

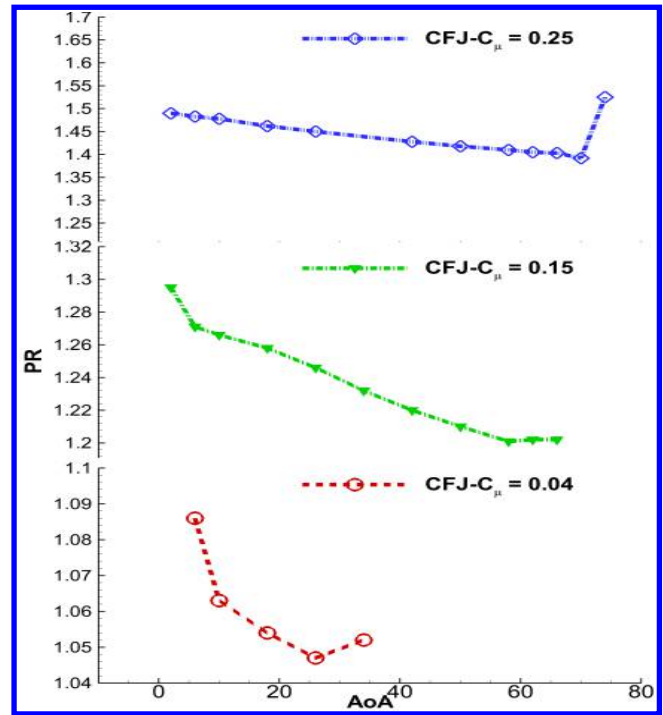


Figure 18: Total pressure ratio PR for the CFJ6421-SST016-SUC053-INJ009 airfoil.

total pressure ratio PR is reduced as well.

Fig. 19 shows the relationship between the lift coefficient and momentum coefficient C_μ for the same airfoil. At low C_μ , the maximum lift coefficient C_{Lmax} linearly increases with the C_μ . As $C_\mu > 0.35$, the maximum lift

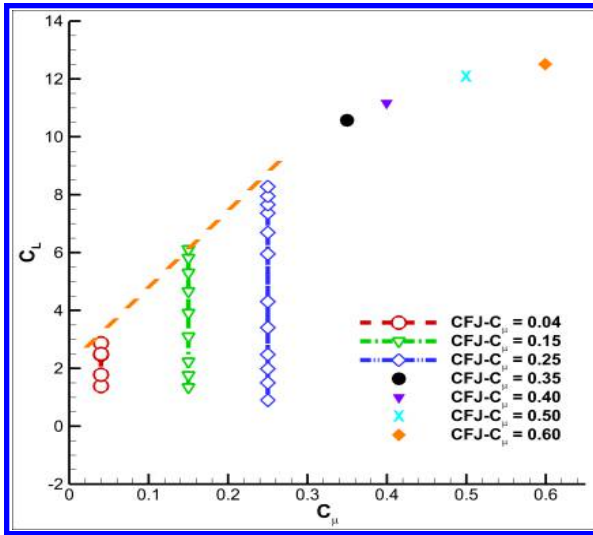


Figure 19: The lift coefficient C_L at different C_μ for the CFJ6421-SST016-SUC053-INJ009 airfoil.

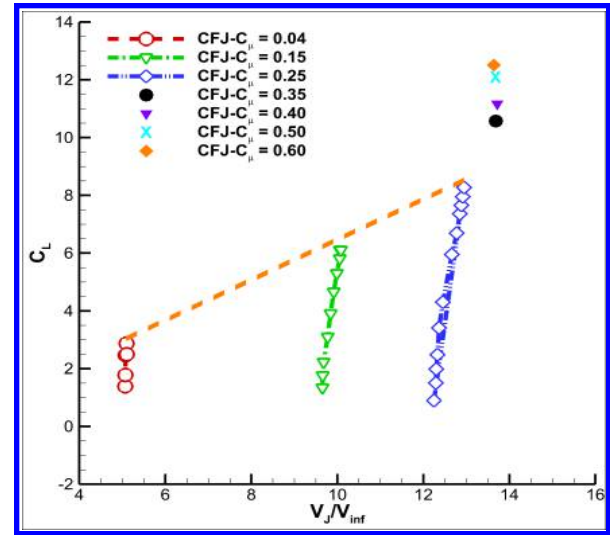


Figure 20: The jet velocity V_J/V_{inf} at different C_μ for the CFJ6421-SST016-SUC053-INJ009 airfoil.

coefficient becomes plateaued. The relationship between the lift coefficient and CFJ jet velocity at different C_μ is shown on Fig. 20. For the same C_μ , it indicates that the injection jet velocity increases monotonically with increasing AoA. For $C_\mu < 0.25$, the maximum lift coefficient linearly grows with the jet velocity and momentum coefficient. For $C_\mu \geq 0.35$, the jet velocity becomes constant at choked condition in the injection slot.

5.1.2 C_{Lmax} Relationship with the CFJ Power Coefficient

It is important to understand what parameter can best correlate with the maximum lift coefficient to guide future engineering design. To achieve such a correlation, the results of all the different CFJ airfoils in the trade study are used, including the configurations to achieve high C_{Lmax} for takeoff/landing and high cruise efficiency with different SST and injection/suction size as listed in Table 4.

Fig. 21 is the variation of C_{Lmax} against C_μ . The linear growth of C_{Lmax} is observed at lower C_μ . The C_{Lmax} reaches a limit as the C_μ further increases. This observation matches to the variation of C_{Lmax} with the C_μ for a cylinder as reported by NASA [9]. However, the data are fairly scattered.

The relationship between C_{Lmax} and mass-averaged jet velocity at the injection slot is shown in Fig. 22. At lower jet velocity, the maximum lift coefficient grows linearly with the jet momentum. When the C_μ is greater than 0.35, the flow is choked at the jet injection, and the jet velocity becomes constant at about $V_J/V_{ref} \approx 14$ (Mach ≈ 0.9). The C_{Lmax} continues to increase after the flow is choked. The reason is that the increased injection total pressure $P_{t_{inj}}$ also increase the jet flow density, hence the momentum coefficient. Similar to the relationship between C_{Lmax} and C_μ , the data are also fairly scattered.

The relationship between the maximum lift coefficient C_{Lmax} and power coefficient P_c for different CFJ airfoils are shown in Fig. 23. The data collapse very well with the variation of P_c . It indicates that at a low power coefficient, the C_{Lmax} grows linearly with the increasing power coefficient P_c . The C_{Lmax} tends to reach a plateau of 14.0 as power coefficient P_c continues to increase. This is the same phenomenon as that observed by Tokumaru and Dimotakis [8] for their rotating cylinder result. When C_L is very high, it is beyond the capability of the flow control to add more energy to the main flow effectively due to very severe adverse pressure gradient. The lift

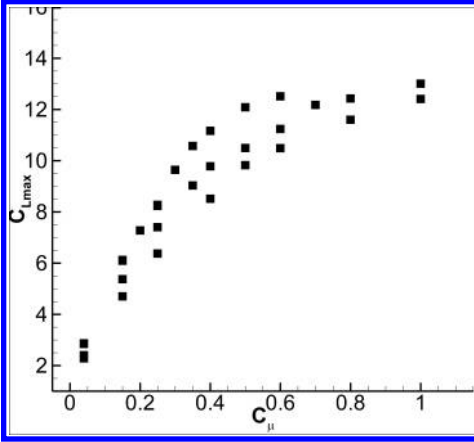


Figure 21: Variation of C_{Lmax} with C_{μ} for different CFJ airfoils.

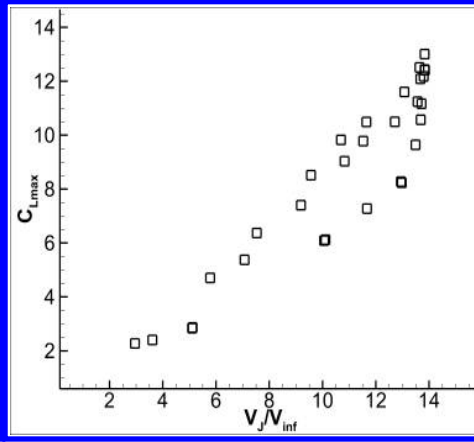


Figure 22: Variation of C_{Lmax} with V_J/V_{inf} for different CFJ airfoils.

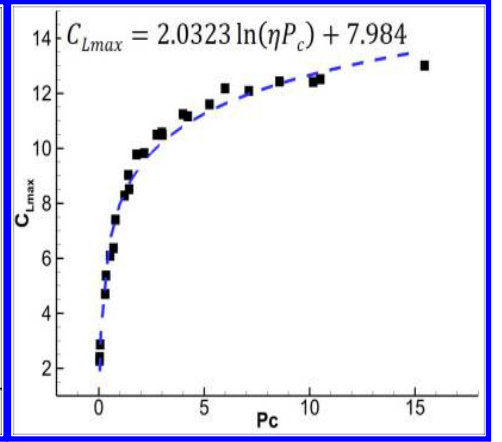


Figure 23: Variation of C_{Lmax} with P_c for different CFJ airfoils.

coefficient increase hence becomes insensitive to the increasing P_c . To obtain the same C_{Lmax} increment, a much higher energy expenditure needs to be paid at a higher C_{Lmax} value than at a lower C_{Lmax} value. How to make an AFC to achieve the highest C_{Lmax} at the lowest energy expenditure is a very interesting and challenging research topic.

The natural logarithm function is used to fit the computational data.

$$C_{Lmax} = C_1 \ln(\eta P_c) + C_2 \quad (14)$$

where η is the CFJ pumping efficiency, $C_1=2.0323$ and $C_2=7.984$ for this airfoil. The correlation of Eq. (14) may only apply to this airfoil thickness of 21%, freestream Mach number of 0.063 and Reynolds number. In other words, the airfoil thickness, Mach number, Reynolds number and some other flow properties are expected to be a part of the parameters for a more general C_{Lmax} correlation.

5.1.3 Flow Field and Vortex Structures

Fig. 24 shows the computed airfoil surface pressure coefficient C_p for the baseline and the CFJ profile at their stall AoA of 18° and 70° at $C_{\mu} = 0.25$ and 0.35 . A spike occurs at the injection slots as the C_p is measured on discontinuous wall surfaces. For the CFJ airfoil, a super-suction occurs at the airfoil leading edge with very low pressure value shown by the high peak value of 80 to 100 for the $-C_p$.

The airfoil surface isentropic Mach number distributions for the baseline and CFJ6421-SST016-SUC053-INJ009 airfoil at $C_{\mu} = 0.25$ and 0.35 are plotted in Fig. 25. The baseline airfoil accelerates the flow from freestream Mach number of 0.063 to the suction peak Mach number of 0.15, whereas the CFJ airfoil reaches the peak Mach number of near 0.8.

The static pressure contour is plotted in Fig. 26. The super-suction effect is displayed on the leading edge of the airfoil with a very low static pressure.

For the maximum lift of 8.2 and 10.6 at $C_{\mu} = 0.25$ and 0.35 respectively at AoA= 70° , the Mach contours and streamlines are shown in Fig. 27. The upstream flow follows airfoil surface, turns around the LE for nearly 180° , and is nicely attached to the suction surface due to the strong induction effect from the high momentum co-flow jet.

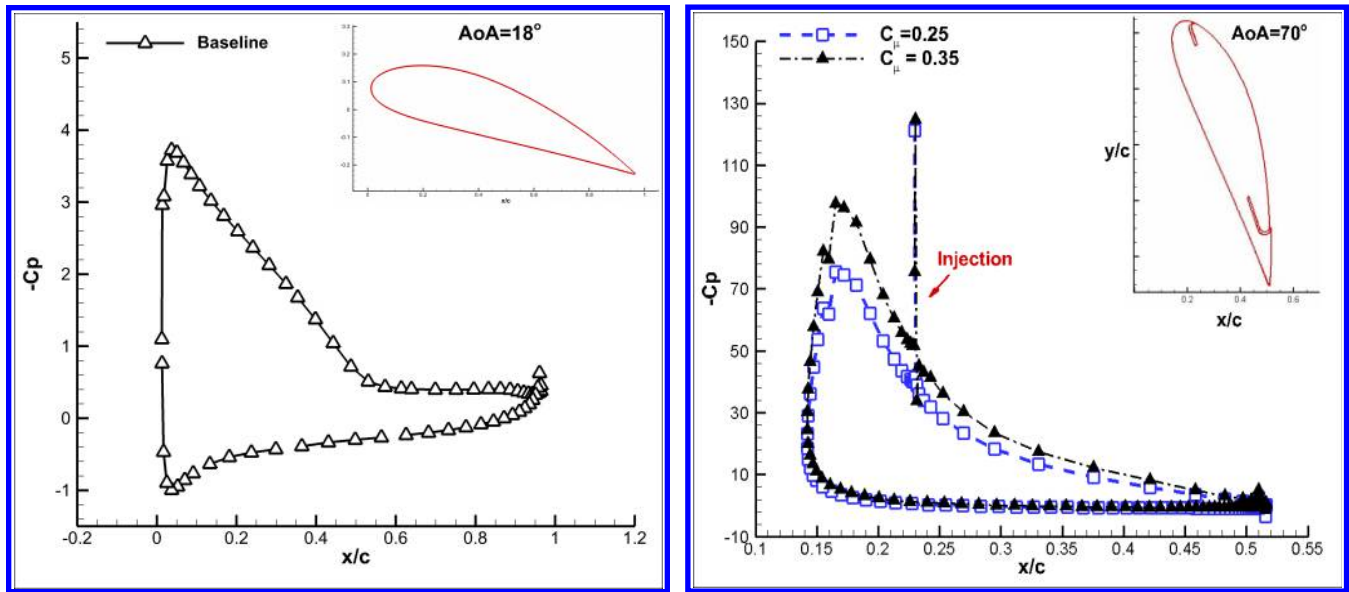


Figure 24: Surface pressure coefficient C_p distribution for the baseline airfoil at $AoA=18^\circ$ (left) and CFJ6421-SST016-SUC053-INJ009 airfoil at $AoA=70^\circ$, $C_\mu = 0.25$ and 0.35 (right).

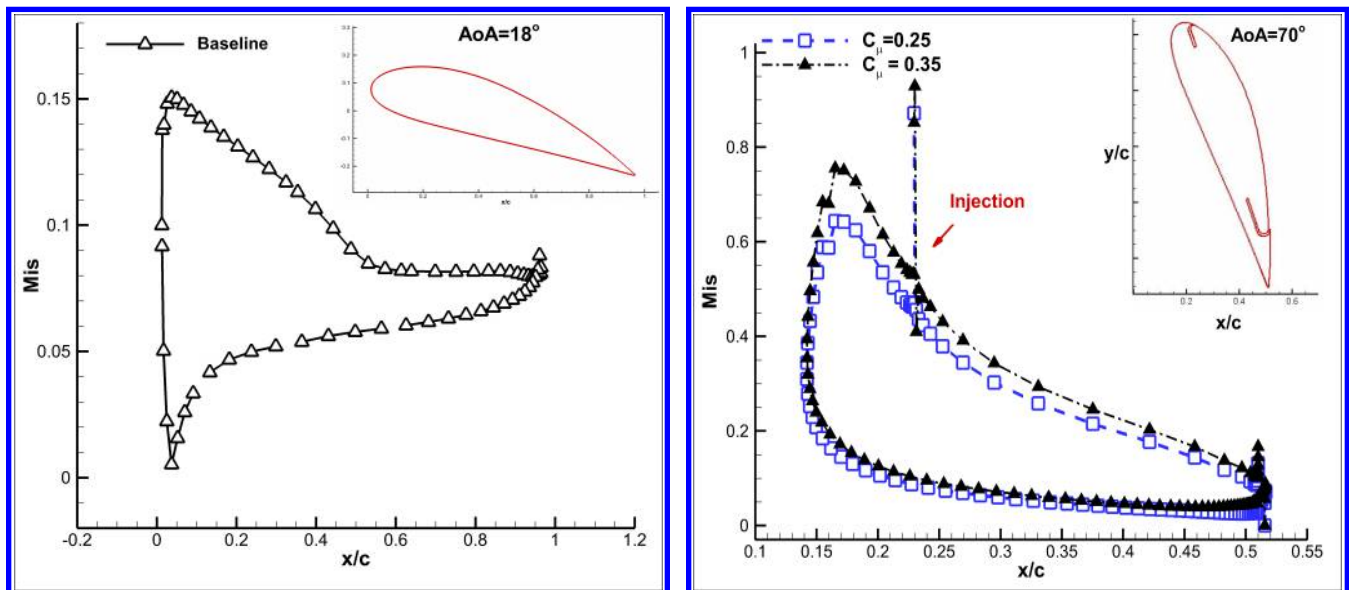


Figure 25: Surface isentropic Mach number M_{is} distribution for the baseline(left) and CFJ6421-SST016-SUC053-INJ009 airfoil(right).

The circulation generating the super-lift coefficient is so high that the stagnation point is detached from the airfoil as shown in Fig. 28 with $C_\mu=0.35$. The very high velocity core occurs near the leading edge within the super suction region. The injection jet is choked at the slot, becomes supersonic within a small region immediately downstream of the injection slot, and turns to subsonic across a normal shock wave, as can be seen in the zoomed plot on the left upper plot in Fig. 28. The flow outside of the jet remains subsonic. This high momentum jet plays the major induction role to make the flow attached.

At the trailing edge, a large clock-wise vortex detaches the stagnation point from the airfoil surface as shown

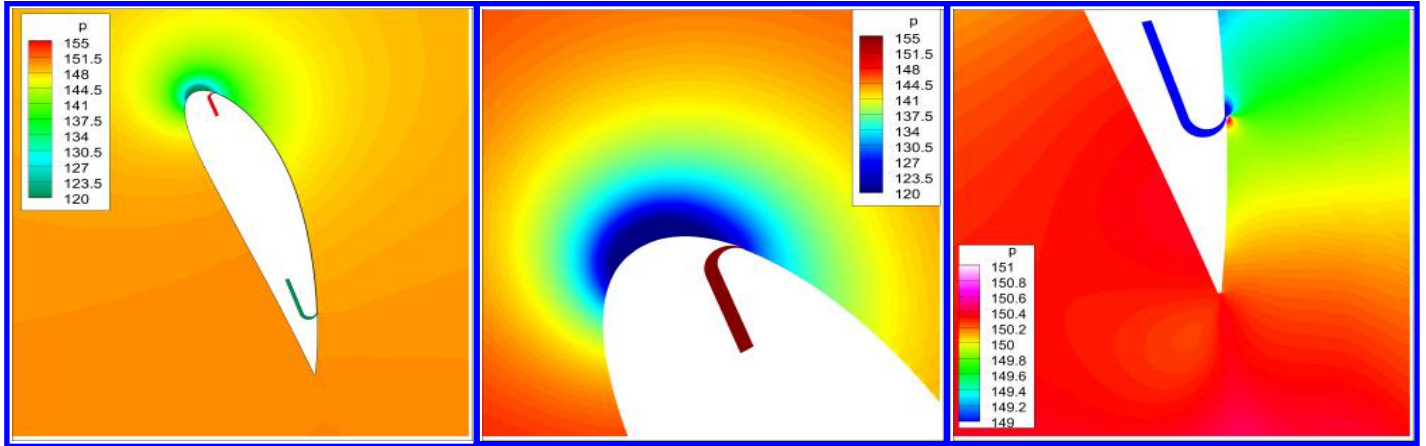


Figure 26: Static pressure distribution at $C_\mu = 0.35$ and $\text{AoA} = 70^\circ$ for the CFJ6421-SST016-SUC053-INJ009 airfoil.

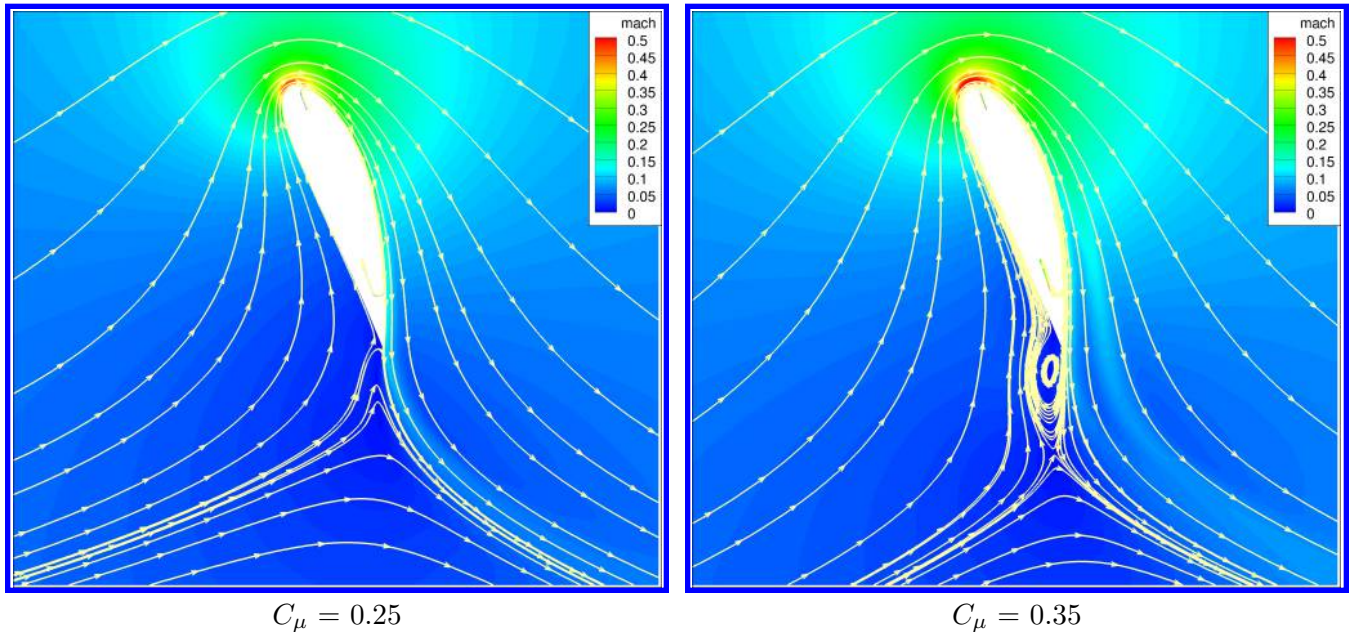


Figure 27: Mach number contours and streamlines at the momentum coefficient $C_\mu = 0.25$ (left) and 0.35 (right) and $\text{AoA} = 70^\circ$ for the CFJ6421-SST016-SUC053-INJ009 airfoil.

in the lower left plot of Fig. 28. The trailing edge vortex creates an extended virtual solid body to form a high pressure region due to the stagnant flow to support the airfoil with super-lift coefficient.

The vorticity contours at $C_\mu = 0.35$, $C_L = 10.6$, and $\text{AoA} = 70^\circ$ is plotted in Fig. 29, which shows that there are four vortex layers starting from the airfoil leading edge. Fig. 30 gives a sketch to more clearly explain the vortex structures. The near-wall surface region bounded by the non-slip wall boundary generates a clock-wise boundary layer vortex sheet. There is a mixing shear layer shed at the lip of the injection duct from the upstream leading edge boundary layer. Between the high momentum CFJ and the shear layer, a counter-clockwise CFJ vortex layer is generated downstream the CFJ injection slot. Next to the injection jet mixing layer is a clockwise vortex layer, which is induced by the CFJ via the mixing layer, named induced vortex layer. The induced vortex layer further induces a high speed jet turning around the leading edge, named as secondary induced jet, which can be clearly

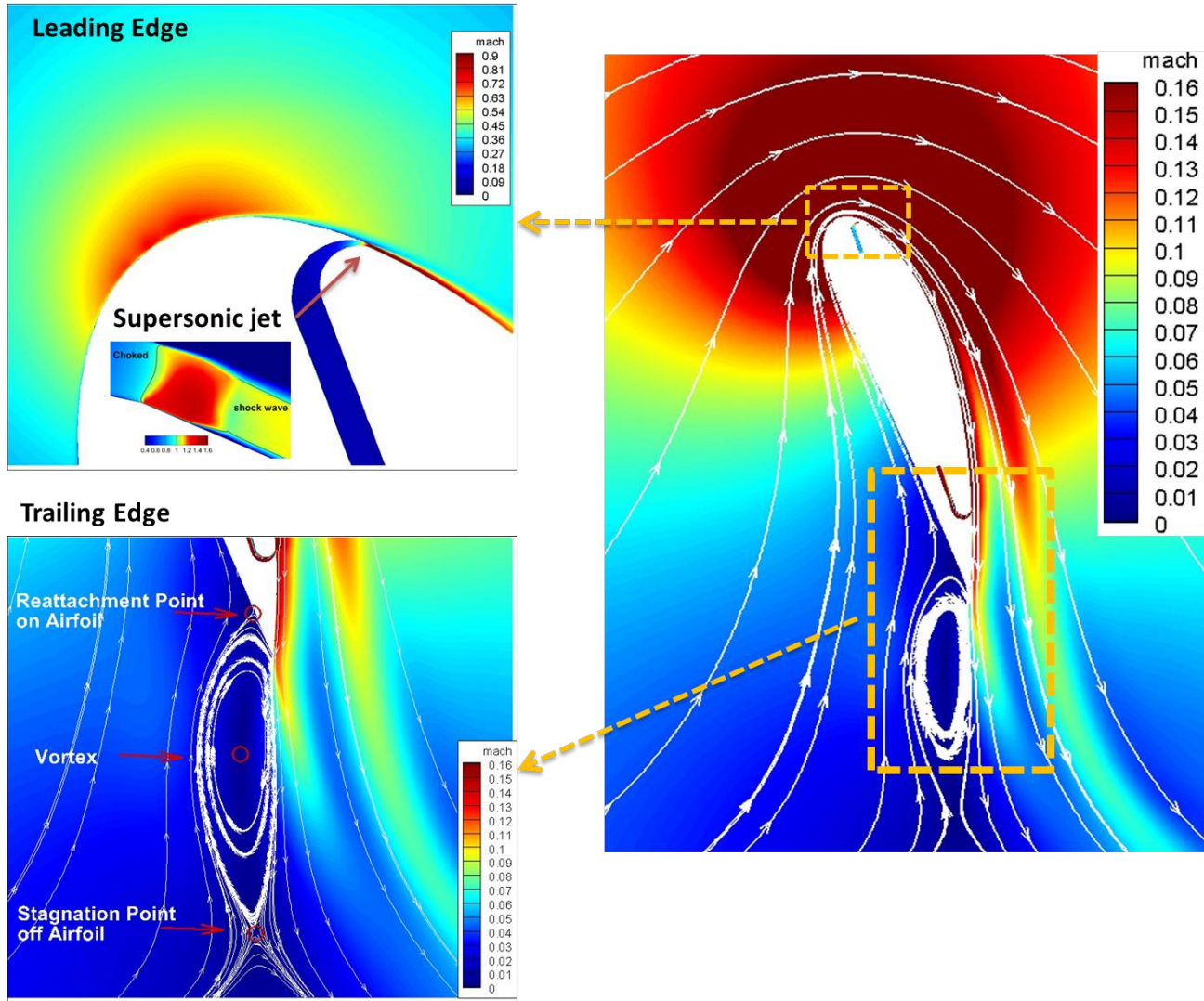


Figure 28: Mach number contours and streamlines at $C_{\mu} = 0.35$ and $\text{AoA} = 70^\circ$ for the CFJ6421-SST016-SUC053-INJ009 airfoil.

seen in Fig. 29 shown by the jet in green color next to the induced vortex layer. The high speed secondary induced jet creates a counter clockwise vortex layer to transit the velocity radially to the slower freestream velocity. The last vortex layer is hence named transitional vortex layer. These complex vortex structures appear to be very similar to the attached leading edge vortex structures of bird wing at powered downstroke, which also has very high angle of attack due to the relative flow direction and generates super-suction effect to provide lift and thrust for bird flight.

The C_{Lmax} appears to have no limit. The C_{Lmax} limit from the potential flow is the result of imposing Kutta condition, which is necessary for potential flow, but not a true physical condition that realistic flows must satisfy as shown in Fig. 28. In reality, C_{Lmax} depends on how much energy can be added to the flow, which varies with the active flow control method.

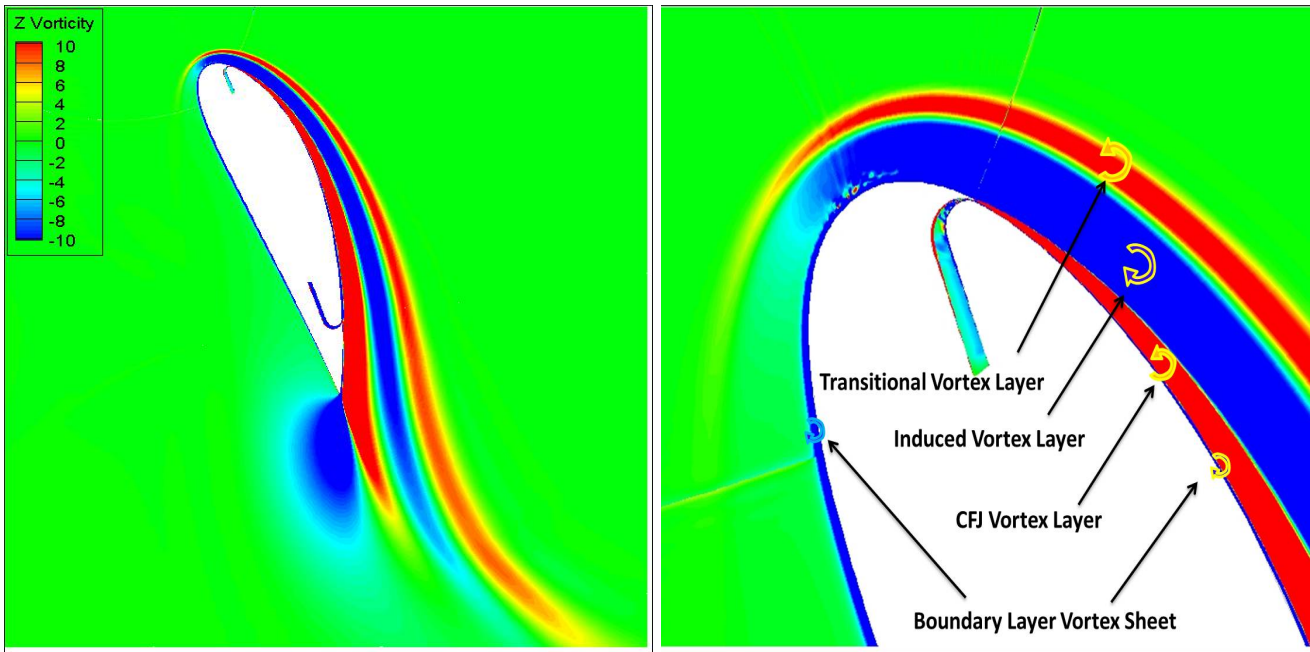


Figure 29: Vorticity contour at $C_{\mu} = 0.35$ and $\text{AoA} = 70^\circ$ for the CFJ6421-SST016-SUC053-INJ009 airfoil.

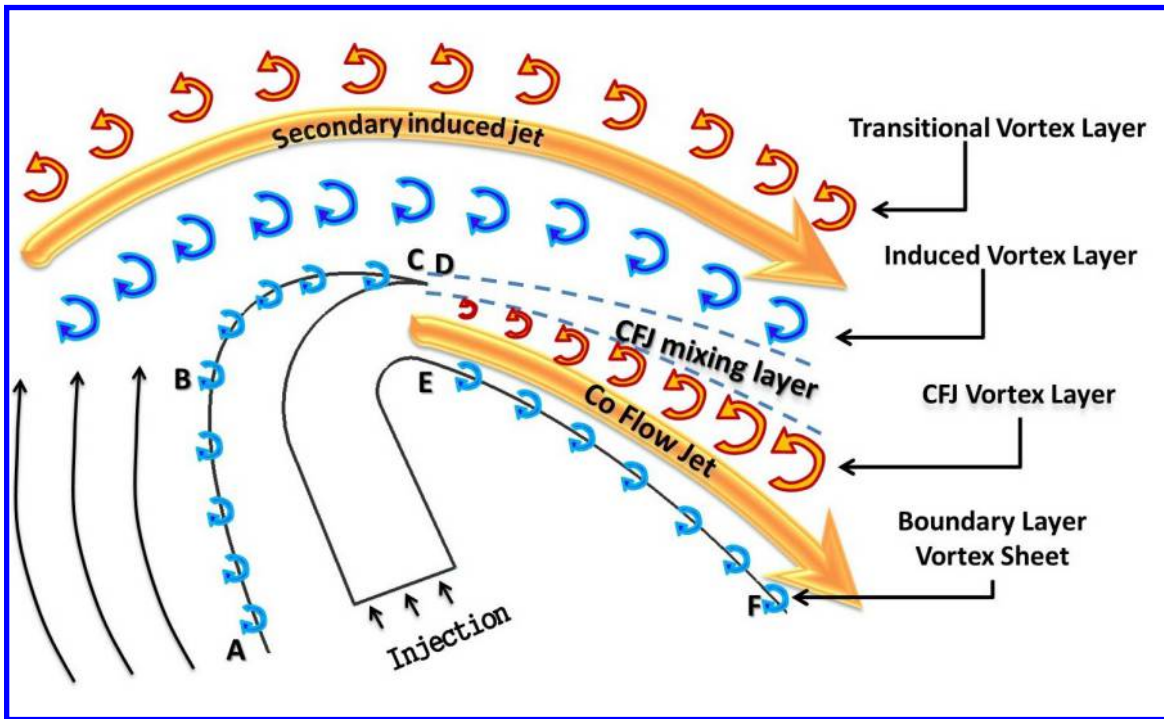


Figure 30: Sketch of the vortex distribution near the leading edge of CFJ airfoil at $C_{\mu} = 0.35$ and $\text{AoA} = 70^\circ$.

5.2 Cruise Efficiency

For transport aircraft, cruise efficiency is crucial. It is desirable to use the same set of airfoil with minimal geometry variation. This section is to present how the geometry variation can benefit the airfoil for high efficiency cruise condition. In general, at cruise condition, the injection slot size is larger and the C_μ is at low level such as 0.02 to 0.06, which minimizes the CFJ power consumption and maximizes the aerodynamic efficiency and productivity efficiency. For the cruise condition, the Mach number of 0.15 and Reynolds number of 2.6 million are used as the freestream conditions. A redesigned CFJ6421-SST143-SUC133-INJ065 airfoil based on NACA6421 airfoil with leading edge modification is used for the cruise configuration [38]. Compared with the previous airfoil CFJ6421-SST016-SUC053-INJ009 for maximum lift coefficient, this cruise airfoil has the SST increased from 0.16% C to 1.43% C , injection slot size increased form 0.09% C to 0.65% C , and suction slot size increased from 0.53% C to 1.33% C . The leading edge radius is slightly reduced to adjust the injection slot location where the lowest static pressure occurs to minimize the CFJ power consumption. All the simulation parameters are summarized in Table 6.

Table 6: Cruise simulation parameters

CFJ6421 airfoil	Mach number	Reynolds number	AoA	C_μ
SST143-SUC133-INJ065	0.15	2,600,000	2°-26°	0.02, 0.04, 0.06

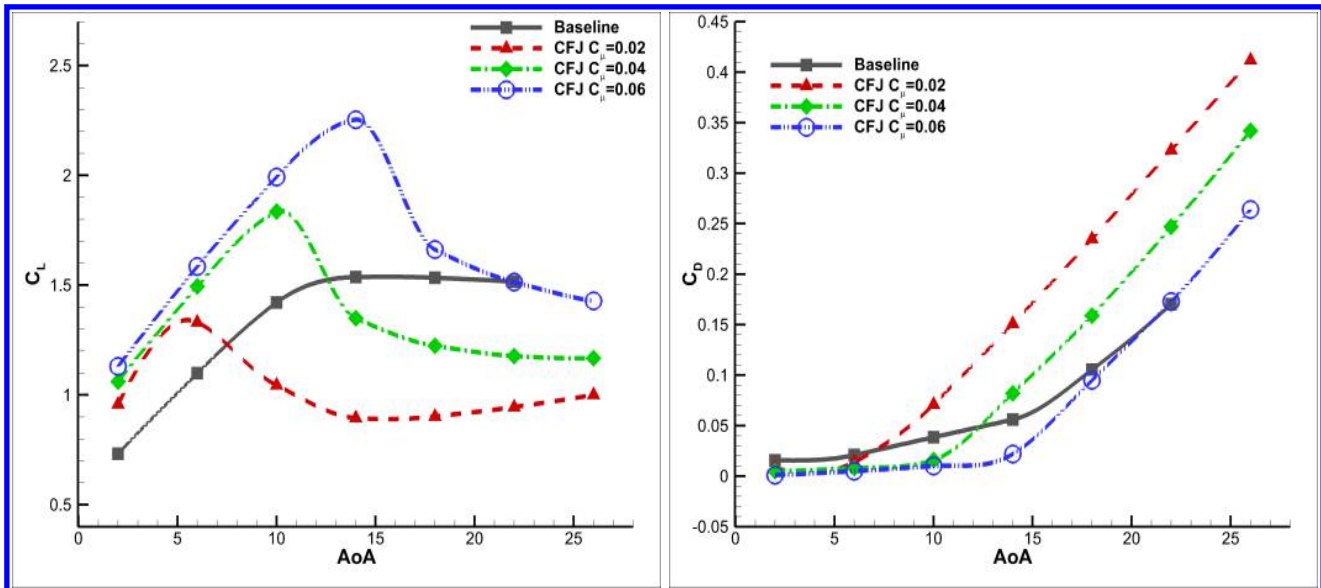


Figure 31: Lift and drag coefficient vs AoA at different C_μ for the baseline and CFJ6421-SST143-SUC133-INJ065 airfoil.

The computed lift and drag coefficient is displayed in Fig. 31. Comparing to the previous design, for the same C_μ , the stall AoAs and maximum lift coefficient are lower because the larger injection slot size generates smaller jet velocity. For a very low C_μ such as 0.02, the stall AoA is smaller than the baseline NACA6421 airfoil. The drag coefficient of CFJ airfoil is also reduced. For a high C_μ of 0.06 at low AoA, negative C_D (thrust generation) is obtained. The drag polar of C_L and C_D is plotted in Fig. 32. It shows that the CFJ airfoil can cruise at $C_L \geq 1.5$ with a near zero drag or a thrust. With such a lift coefficient, the baseline airfoil is already stalled.

The moment coefficient is displayed in Fig. 33. The CFJ airfoil nose-down moment coefficient is higher than the baseline airfoil for all the C_μ , but is substantially reduced when the AoA is increased to near the AoA of C_{Lmax} .

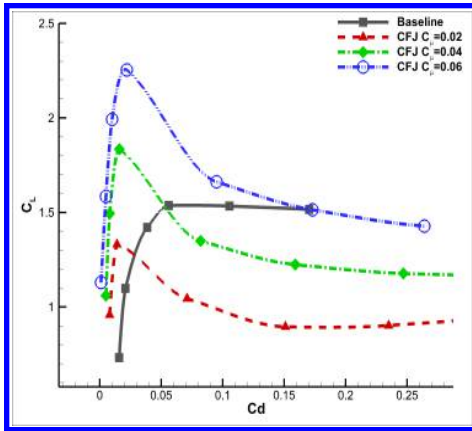


Figure 32: Drag polar at different C_μ for the baseline and CFJ6421-SST143-SUC133-INJ065 airfoil.

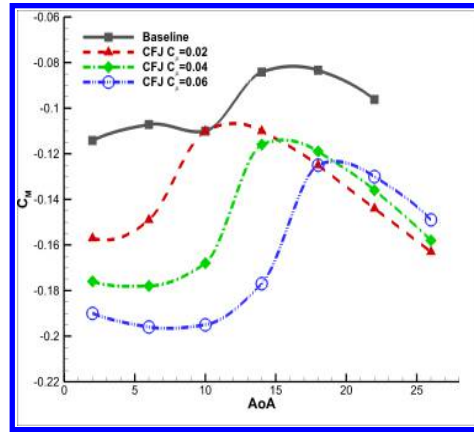


Figure 33: Moment coefficient C_M vs AoA at different C_μ for the baseline and CFJ6421-SST143-SUC133-INJ065 airfoil.

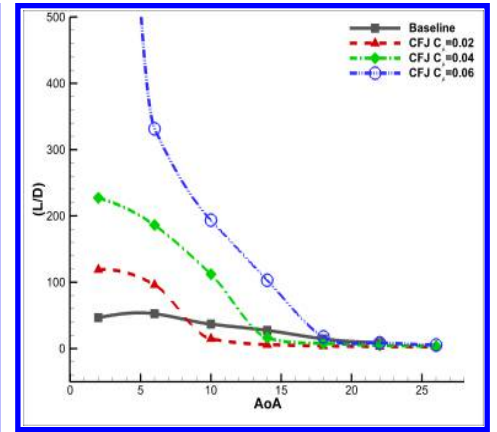


Figure 34: Aerodynamic efficiency (L/D) vs AoA at different C_μ for the baseline and CFJ6421-SST143-SUC133-INJ065 airfoil.

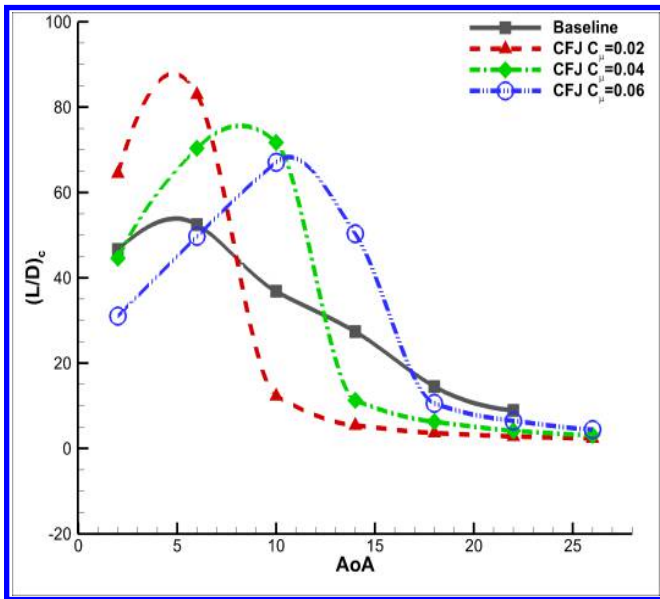


Figure 35: Corrected aerodynamic efficiency $(L/D)_c$ vs AoA at different C_μ for the baseline and CFJ6421-SST143-SUC133-INJ065 airfoil.

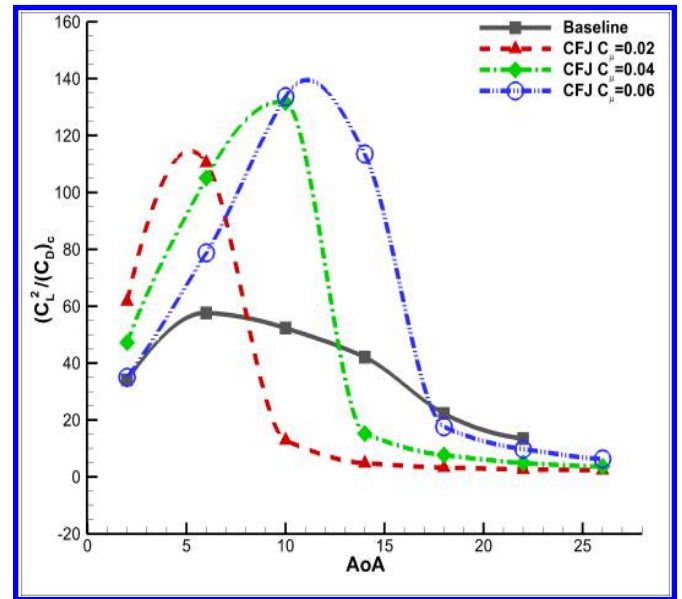


Figure 36: Corrected productivity efficiency $(C_L^2/C_D)_c$ vs AoA at different C_μ for the baseline and CFJ6421-SST143-SUC133-INJ065 airfoil.

The ratio of lift to drag is shown in Fig. 34. The CFJ airfoil has extremely high L/D because the CFJ airfoil generates thrust. The corrected aerodynamic efficiency coefficient $(L/D)_c$ is plotted in Fig. 35. For the baseline airfoil, the maximum L/D is 53 at $AoA=6^\circ$. For the CFJ airfoil at all the C_μ , the maximum $(L/D)_c$ is higher and up to 83 with an increase from 28% at $C_\mu = 0.06$ to 62% at $C_\mu = 0.02$. Compared with Fig. 15 for the takeoff/landing airfoil configuration with smaller injection size, the maximum $(L/D)_c$ is more than tripled.

The corrected productivity efficiency $(C_L^2/C_D)_c$ for the CFJ and baseline airfoil is plotted in Fig. 36. Due to the high lift enhancement of CFJ, the productivity coefficient is much higher than that of the baseline airfoil, with

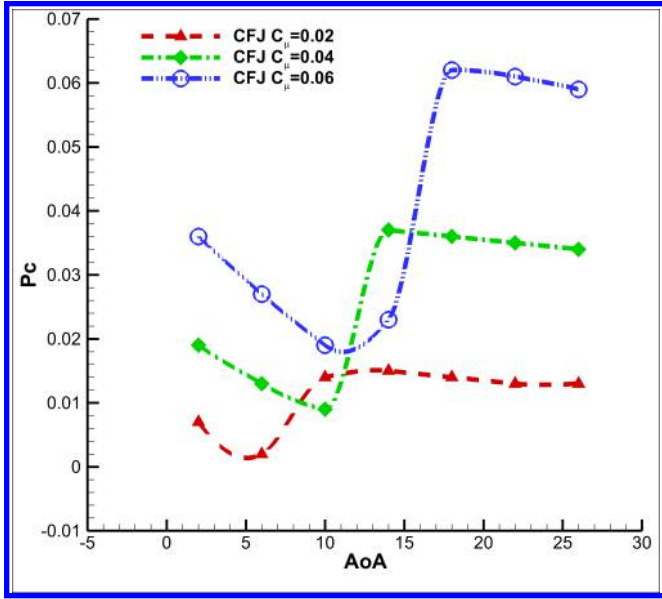


Figure 37: Power coefficient P_c vs AoA at different C_μ for the CFJ6421-SST143-SUC133-INJ065 airfoil.

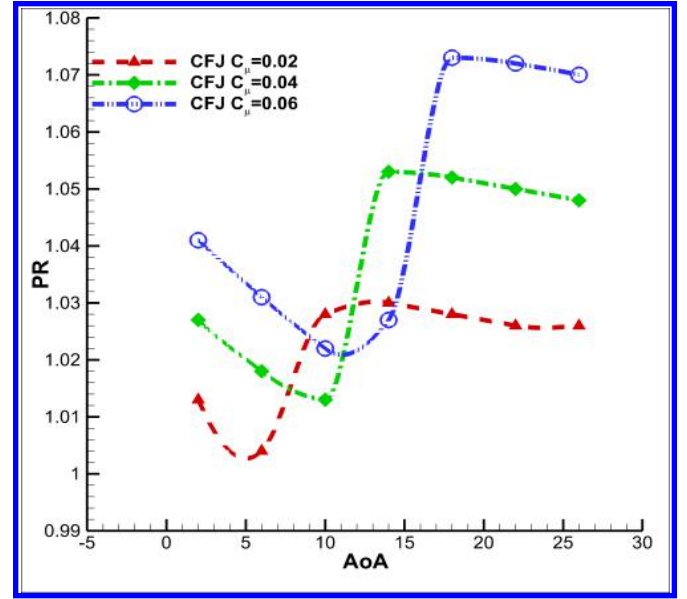


Figure 38: Total pressure ratio PR vs AoA at different C_μ for the CFJ6421-SST143-SUC133-INJ065 airfoil.

an increase of 98% at $C_\mu = 0.02$ to 141% at $C_\mu = 0.06$. The substantially increased aerodynamic efficiency and productivity efficiency are all attributed to that the CFJ airfoil is able to achieve significant lift increase and drag reduction at low AoA with very low energy expenditure as shown in Fig. 37 and 38. This provides the CFJ airfoil a unique feature that it can be used for both high efficiency cruise and high lift takeoff/landing.

Table 7: Comparison of parameters for baseline and CFJ airfoils at the best aerodynamic efficiency point $(L/D)_{c_{max}}$. (CFJ pumping efficiency $\eta = 100\%$)

Airfoil	AoA	C_L	P_c	(L/D)	$(L/D)_{c_{max}}$	$(C_L^2/C_D)_{c_{max}}$	C_M
Baseline	6	1.098	-	52.496	52.496	57.672	-0.107
CFJ, $C_\mu=0.02$	6	1.331	0.002	96.134	82.954	110.420	-0.149
CFJ, $C_\mu=0.04$	10	1.835	0.009	112.057	71.744	131.629	-0.168
CFJ, $C_\mu=0.06$	10	1.993	0.019	193.553	67.109	133.743	-0.195

Table 7 summarizes the comparison of aerodynamic efficiency performance obtained for the baseline and CFJ airfoils at different C_μ with the CFJ pumping efficiency assumed to be 100%. For the baseline airfoil, the most efficient point with the maximum $(L/D)_{max}$ of 52.496 is obtained at AoA=6°. At this condition, the lift coefficient is 1.098 and the moment coefficient is -0.107. For the CFJ airfoil at $C_\mu = 0.02$, the maximum $(L/D)_{c_{max}}$ ratio of 82.954 is obtained at AoA=6°. The pure aerodynamic efficiency is enhanced to 96.134. The CFJ airfoil also achieves higher C_L of 1.331 and higher nose-down moment coefficient of C_M of -0.149. At higher C_μ of 0.04 and 0.06, the AoA of maximum $(L/D)_{c_{max}}$ ratio is shifted to 10°. The $(L/D)_{c_{max}}$ drops with the increase of C_μ . With the higher AoA and C_μ , the lift coefficient is increased. As a result of higher C_L , the maximum $(C_L^2/C_D)_{c_{max}}$ increases to 133.743. The moment coefficient C_M are higher at the higher C_μ .

To consider the realistic CFJ pumping energy loss, a CFJ pumping efficiency of 80% is used and the comparison of aerodynamic performance is given in Table 8. Based on Eq. (7), the required CFJ power consumption is higher for lower pumping efficiency. Even with the 80% CFJ pumping efficiency, the aerodynamic efficiency $(L/D)_{c_{max}}$ and

Table 8: Comparison of parameters for CFJ airfoils at the best aerodynamic efficiency point $(L/D)_{c_{max}}$. (CFJ pumping efficiency $\eta = 80\%$)

Airfoil	AoA	C_L	P_c	(L/D)	$(L/D)_{c_{max}}$	$(C_L^2/C_D)_{c_{max}}$	C_M
Baseline	6	1.098	-	52.496	52.496	57.672	-0.107
CFJ, $C_\mu=0.02$	6	1.331	0.0028	96.134	80.204	106.761	-0.149
CFJ, $C_\mu=0.04$	10	1.835	0.0115	112.057	65.824	120.767	-0.168
CFJ, $C_\mu=0.06$	10	1.993	0.0243	193.553	57.688	114.967	-0.195

productivity efficiency $(C_L^2/C_D)_{c_{max}}$ are still substantially higher than those of the baseline airfoil. The maximum aerodynamic efficiency $(L/D)_{c_{max}}$ is 80.204 at $C_\mu=0.02$, a 53% increase. More importantly, the productivity efficiency $(C_L^2/C_D)_{c_{max}}$ is 120.767 at $C_\mu=0.04$, an increase of 109%. It means that the transportation capability of the CFJ airfoil is doubled with the same energy consumption.

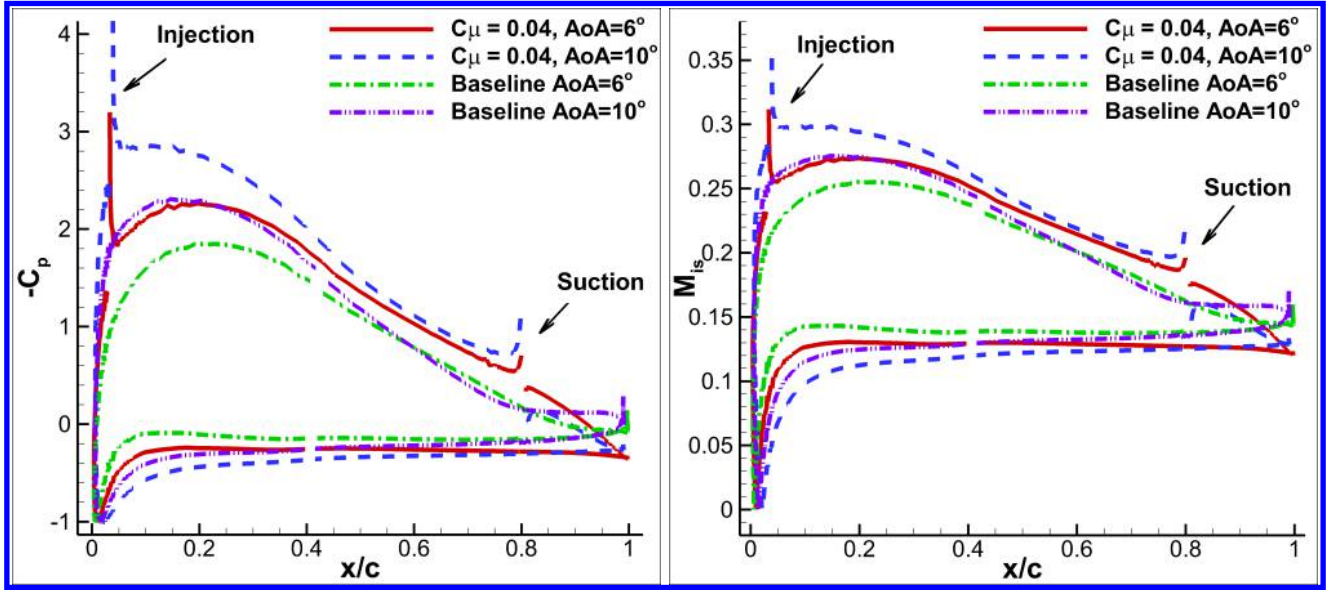


Figure 39: Surface pressure coefficient C_p (left) and isentropic Mach number M_{is} (right) distribution for the baseline and CFJ6421-SST143-SUC133-INJ065 airfoil at $C_\mu=0.04$ and AoA = 6° , 10° .

Fig. 39 shows the computed surface pressure coefficient C_p and the isentropic Mach number M_{is} for the baseline and the CFJ airfoil at $C_\mu = 0.04$ and AoA at 6° and 10° . The surface loading of the CFJ airfoil is significantly higher than the baseline airfoil, resulting a substantially higher lift coefficient.

Fig. 40 is the Mach number contours at AoA= 10° for the baseline airfoil and CFJ airfoil at $C_\mu=0.04$ and AoA = 6° and 10° . The trailing edge of the baseline airfoil has a small separation due to the high thickness of the airfoil. All the separation is removed by using the CFJ airfoil. And on the suction surface, the high velocity area and velocity magnitude are increased by the CFJ airfoil.

The pressure contours for the baseline and CFJ airfoil at $C_\mu=0.04$, AoA= 6° , 10° are shown in Fig. 41. Because of the higher acceleration on the suction surface of the CFJ airfoil, the low pressure area is larger.

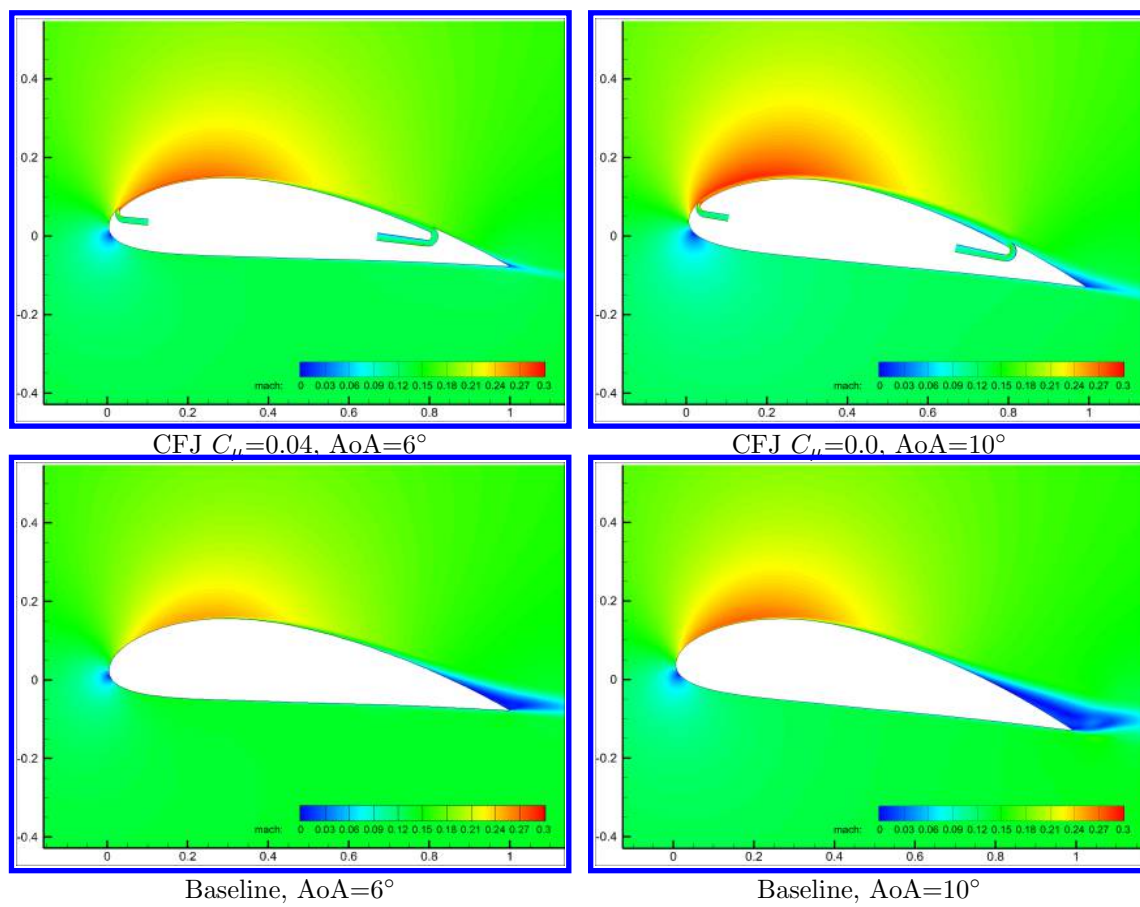


Figure 40: Mach number contours at AoA = 6°, 10° for baseline(bottom) and CFJ6421-SST143-SUC133-INJ065 airfoil(top).

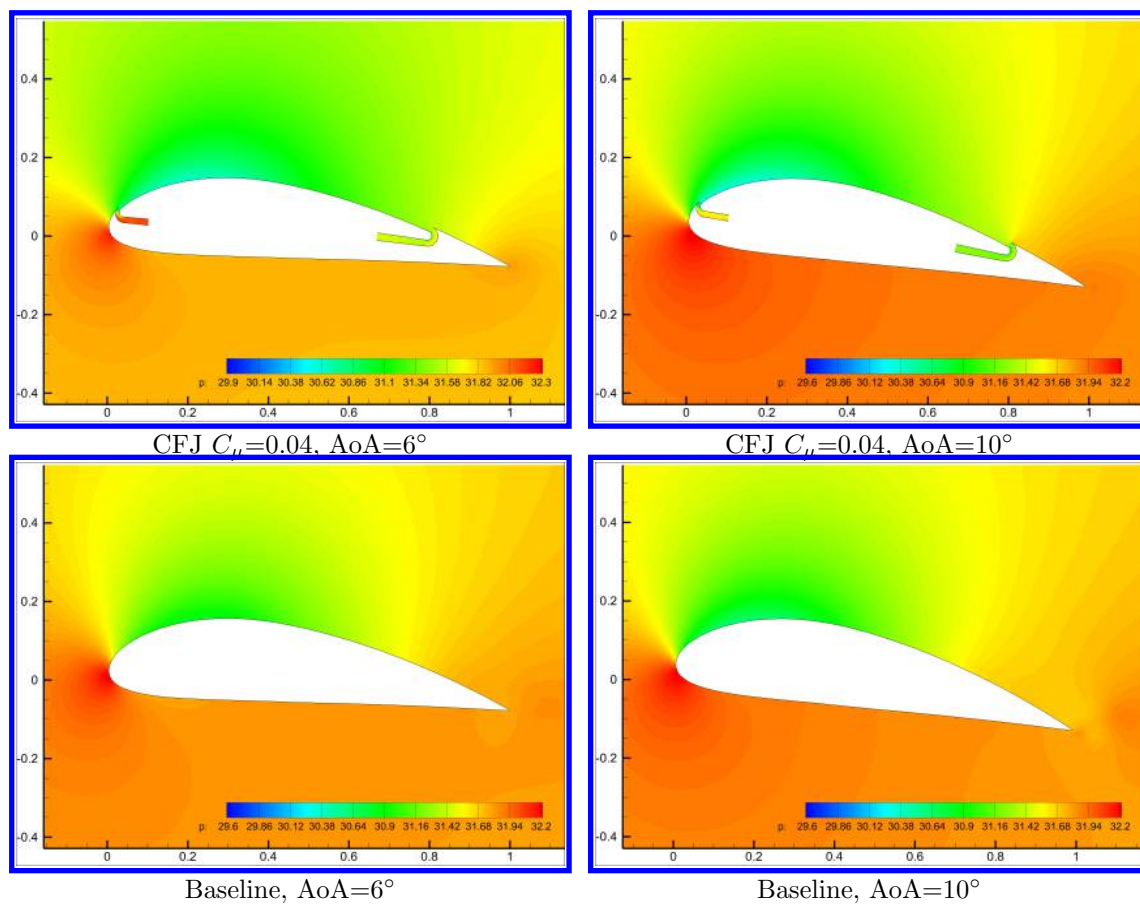


Figure 41: Static pressure contours at AoA = 6°, 10° for baseline(bottom) and CFJ6421-SST143-SUC133-INJ065 airfoil(top).

6 Conclusion

The present numerical study indicates that CFJ active flow control airfoil is able to achieve the maximum lift coefficient far exceeding the theoretical limit at a very high AoA up to 70° . At the same time, CFJ airfoil is also able to substantially increase the cruise aerodynamic efficiency and productivity efficiency at low AoA due to its increased lift, reduced drag, and very low energy expenditure.

Two CFJ airfoil configurations are created from the baseline NACA 6421 airfoil by translating the suction surface downward and adjusting the injection and suction slot sizes. One CFJ airfoil with smaller injection size is to achieve high C_{Lmax} for takeoff and landing. The other CFJ airfoil with larger injection size is to achieve high cruise efficiency. The first CFJ airfoil (CFJ6421-SST016-SUC053-INJ009) has the suction surface translation of 0.16% C, injection slot size of 0.09% C, and suction slot size of 0.53% C. The maximum lift coefficient of 12.6 is achieved at AoA= 70° , M=0.063 and $C_\mu = 0.60$. It is 66% higher than the theoretical limit of 7.6 for a 21% thickness airfoil. The circulation achieved around the CFJ airfoil is so high that the stagnation point is detached from the airfoil solid body and the Kutta condition does not apply anymore. For the super-lift condition at AoA of 70° , the vortex structures in the CFJ injection region appear to include 4 vortex layers next to each other from the airfoil wall surface to the far field freestream : 1) clockwise boundary layer vortex sheet on the airfoil suction surface downstream of the injection slot; 2) counter clockwise CFJ vortex layer due to the high momentum jet and the shear layer shed from the upstream leading edge boundary layer; 3) clockwise induced vortex layer induced by the high momentum co-flow jet via the mixing shear layer. Next to the induced vortex layer is a high momentum secondary induced jet; 4) the last vortex layer is a counter clockwise vortex layer, through which the secondary induced jet transits to the slower freestream velocity.

The C_{Lmax} appears to have no limit. The C_{Lmax} limit from the potential flow is the result of imposing Kutta condition, which is necessary for potential flow, but not a true physical condition that realistic flows must satisfy. In reality, C_{Lmax} depends on how much energy can be added to the flow, which varies with the active flow control method. This study indicates that the C_{Lmax} is correlated very well with the CFJ power coefficient. The C_{Lmax} increase is very sensitive to energy addition when the C_{Lmax} is at low level. There is almost a linear relationship between the C_{Lmax} increase and the CFJ power consumed at low C_{Lmax} level. The C_{Lmax} eventually becomes plateaued even with continuously increased consumption of CFJ power. This is because when the C_{Lmax} is very high, it is very difficult to add more energy to the flow due to the very severe adverse pressure gradient. How to make an AFC to achieve the highest C_{Lmax} at the lowest energy expenditure is a very interesting research topic.

A new parameter named productivity efficiency defined as C_L^2/C_D is introduced to measure the cruise transportation capability of aircraft to carry its total weight for maximum distance. The second CFJ airfoil (CFJ6421-SST143-SUC133-INJ065) is redesigned with slightly modified leading edge radius, and has the SST of 1.43%C, INJ of 0.65% C, and SUC of 1.33 % C. For the second CFJ airfoil with an assumed CFJ pumping efficiency of 80%, the peak aerodynamic efficiency $(L/D)_c$ is about 53% higher than that of the baseline airfoil. The productivity efficiency $(C_L^2/C_D)_c$ of the CFJ airfoil is 109% higher. The CFJ airfoil is demonstrated by validated numerical simulation to be able to achieve super-lift coefficient for ESTOL performance at takeoff/landing at very high angle of attack and ultra-high efficiency for cruise at low angle of attack.

7 Acknowledgment

This project is sponsored by the Defense Advanced Research Projects Agency and monitored by the program manager Jean-Charles Ledé under Cooperative Agreement No.: HR0011-16-2-0052. The content of the information does not necessarily reflect the position or the policy of the Government, and no official endorsement should be

inferred. The simulations are conducted on Pegasus supercomputing system at the Center for Computational Sciences at the University of Miami.

References

- [1] A. O. Smith, "High-lift aerodynamics," *Journal of Aircraft*, vol. 12, no. 6, pp. 501–530, 1975.
- [2] G. J. Couluris, C. Hange, D. Wardwell, D. Signor, and J. Phillips, "A potential impact analysis of estol aircraft on newark airport operations," in *American Institute of Aeronautics and Astronautics Modeling and Simulation Technologies Conference and Exhibit, Hilton Head, SC*, 2007.
- [3] Y. J. and H. D., "Executive summary of calpoly/nasa extreme short takeoff and landing (estol) work.," *SAE International Powered Lift Conference, Warrendale*, 2005.
- [4] G. J. Couluris, D. Signor, and J. Phillips, "Cruise-efficient short takeoff and landing (cestol): Potential impact on air traffic operations," *NASA/CRC2010-216392*, 2010.
- [5] Rudolph, P. K. C., "High-Lift Systems on Commercial Subsonic Airliners." NASA Contractor Report 4746, Sept. 1996.
- [6] T. O. G. Prandtl, Ludwig, *Applied Hydro- and Aeromechanics (Dover Books on Aeronautical Engineering)*. Dover Publications, 1934.
- [7] S. Mittal and B. Kumar, "Flow past a rotating cylinder," *Journal of Fluid Mechanics*, vol. 476, pp. 303–334, 2003.
- [8] P. Tokumar and P. Dimotakis, "The lift of a cylinder executing rotary motions in a uniform flow," *Journal of Fluid Mechanics*, vol. 255, pp. 1–10, 1993.
- [9] V. E. Lockwood, *Lift generation on a circular cylinder by tangential blowing from surface slots*. National Aeronautics and Space Administration, 1960.
- [10] R. J. Englar, "Overview of circulation control pneumatic aerodynamics: blown force and moment augmentation and modification as applied primarily to fixed-wing aircraft," *Reston, VA: American Institute of Aeronautics and Astronautics, 2006.*, pp. 23–68, 2006.
- [11] R. J. Englar, "Circulation Control Pneumatic Aerodynamics: Blown Force and Moment Augmentation and Modifications; Past, Present and Future." AIAA 2000-2541, June 2000.
- [12] G.-C. Zha, W. Gao, and C. Paxton, "Jet Effects on Co-Flow Jet Airfoil Performance," *AIAA Journal, No. 6.*, vol. 45, pp. 1222–1231, 2007.
- [13] G. S. Jones, "Pneumatic Flap Performance for a 2D Circulation Control Airfoil, Steady & Pulsed." *Applications of Circulation Control Technologies*, Chapter 7, p. 191-244, Vol. 214, Progress in Astronautics and Aeronautics, AIAA Book Series, Editors: Joslin, R. D. and Jones, G. S., 2006.
- [14] Greitzer, E. M. and Slater, H. N., "N+3 Aircraft Concept Designs and Trade Studies, Final Report." Final Report, March 31, 2010.
- [15] Hileman, J.I. and Spakovszky, Z.S. and Drela, M. and Sargeant, M.A., "Airframe Design for 'Silent Aircraft'." AIAA Paper 2007-453, 45th AIAA Aerospace Sciences Meeting, Reno, NV, Jan 2007.

- [16] G.-C. Zha and D. C. Paxton, "A Novel Flow Control Method for Airfoil Performance Enhancement Using Co-Flow Jet." *Applications of Circulation Control Technologies*, Chapter 10, p. 293-314, Vol. 214, Progress in Astronautics and Aeronautics, AIAA Book Series, Editors: Joslin, R. D. and Jones, G.S., 2006.
- [17] G.-C. Zha, C. Paxton, A. Conley, A. Wells, and B. Carroll, "Effect of Injection Slot Size on High Performance Co-Flow Jet Airfoil," *AIAA Journal of Aircraft*, vol. 43, 2006.
- [18] G.-C. Zha, B. Carroll, C. Paxton, A. Conley, and A. Wells, "High Performance Airfoil with Co-Flow Jet Flow Control," *AIAA Journal*, vol. 45, 2007.
- [19] Wang, B.-Y. and Haddoukessouni, B. and Levy, J. and Zha, G.-C., "Numerical Investigations of Injection Slot Size Effect on the Performance of Co-Flow Jet Airfoil ," *AIAA Journal of Aircraft*, vol. 45, pp. 2084–2091, 2008.
- [20] B. P. E. Dano, D. Kirk, and G.-C. Zha, "Experimental Investigation of Jet Mixing Mechanism of Co- Flow Jet Airfoil." AIAA-2010-4421, 5th AIAA Flow Control Conference, Chicago, IL, 28 Jun - 1 Jul 2010.
- [21] B. P. E. Dano, G.-C. Zha, and M. Castillo, "Experimental Study of Co-Flow Jet Airfoil Performance Enhancement Using Micro Discreet Jets." AIAA Paper 2011-0941, 49th AIAA Aerospace Sciences Meeting, Orlando, FL, 4-7 January 2011.
- [22] Lefebvre, A. and Zha, G.-C. , "Design of High Wing Loading Compact Electric Airplane Utilizing Co-Flow Jet Flow Control." AIAA Paper 2015-0772, AIAA SciTech2015: 53rd Aerospace Sciences Meeting, Kissimmee, FL, 5-9 Jan 2015.
- [23] Lefebvre, A. and Dano, B. and Bartow, W. and Di Franzo, M. and Zha, G.-C., "Performance Enhancement and Energy Expenditure of Co-Flow Jet Airfoil with Variation of Mach Number." AIAA Paper 2013-0490, AIAA Journal of Aircraft, DOI: 10.2514/1.C033113, 2016.
- [24] Liu, Z.-X. and Zha, G.-C., "Transonic Airfoil Performance Enhancement Using Co-Flow Jet Active Flow Control." AIAA Paper 2016-3066, AIAA Aviation, June 13-17 2016.
- [25] Lefebvre, A. and Zha, G.-C., "Trade Study of 3D Co-Flow Jet Wing for Cruise Performance." AIAA Paper 2016-0570, AIAA SCITECH2016, AIAA Aerospace Science Meeting, San Diego, CA, 4-8 January 2016.
- [26] P. R. Spalart and S. R. Allmaras, "A one-equation turbulence model for aerodynamic flows," in *30th Aerospace Sciences Meeting and Exhibit, Aerospace Sciences Meetings, Reno, NV, USA, AIAA Paper 92-0439*, 1992.
- [27] Y.-Q. Shen and G.-C. Zha, "Large Eddy Simulation Using a New Set of Sixth Order Schemes for Compressible Viscous Terms ," *Journal of Computational Physics*, vol. 229, pp. 8296–8312, 2010.
- [28] Zha, G.C., Shen, Y.Q. and Wang, B.Y., "An improved low diffusion E-CUSP upwind scheme ," *Journal of Computer and Fluids*, vol. 48, pp. 214–220, Sep. 2011.
- [29] Y.-Q. Shen and G.-Z. Zha , "Generalized finite compact difference scheme for shock/complex flowfield interaction," *Journal of Computational Physics*, vol. doi:10.1016/j.jcp.2011.01.039, 2011.
- [30] Shen, Y.-Q. and Zha, G.-C. and Wang, B.-Y., "Improvement of Stability and Accuracy of Implicit WENO Scheme," *AIAA Journal*, vol. 47, No. 2, pp. 331–344, 2009.
- [31] Shen, Y.-Q. and Zha, G.-C. and Chen, X.-Y., " High Order Conservative Differencing for Viscous Terms and the Application to Vortex-Induced Vibration Flows," *Journal of Computational Physics*, vol. 228(2), pp. 8283–8300, 2009.

- [32] Shen, Y.-Q. and Zha, G.-C. , “ Improvement of the WENO Scheme Smoothness Estimator,” *International Journal for Numerical Methods in Fluids*, vol. DOI:10.1002/fld.2186, 2009.
- [33] G.-C. Zha and E. Bilgen, “Numerical Study of Three-Dimensional Transonic Flows Using Unfactored Upwind-Relaxation Sweeping Algorithm,” *Journal of Computational Physics*, vol. 125, pp. 425–433, 1996.
- [34] B.-Y. Wang and G.-C. Zha, “A General Sub-Domain Boundary Mapping Procedure For Structured Grid CFD Parallel Computation,” *AIAA Journal of Aerospace Computing, Information, and Communication*, vol. 5, No.11, pp. 2084–2091, 2008.
- [35] Wang, B. Y and Zha, G.-C. , “Detached-Eddy Simulation of a Co-Flow Jet Airfoil at High Angle of Attack.” AIAA Paper 2009-4015, accepted for publication in *Journal of Aircraft*, 2011.
- [36] Im, H.-S. and Zha, G.-C. and Dano, B. P. E., “Large Eddy Simulation of Coflow Jet Airfoil at High Angle of Attack,” *Journal of Fluid Engineering*, vol. 136(2), p. 021101, 2014.
- [37] Y.-Q. Shen, G.-C. Zha, and B.-Y. Wang, “Improvement of Stability and Accuracy of Implicit WENO Scheme ,” *AIAA Journal*, vol. 47, pp. 331–344, 2009.
- [38] A. M. Lefebvre, “Investigation of co-flow jet flow control and its applications,” 2015.
- [39] J. D. Anderson Jr, *Fundamentals of aerodynamics*. Tata McGraw-Hill Education, 2010.
- [40] J. Chattot and M. Hafez, “Theoretical and applied aerodynamics,” *Theoretical and Applied Aerodynamics: and Related Numerical Methods*, ISBN 978-94-017-9824-2. Springer Science+ Business Media Dordrecht, 2015.

8 Appendix: Lift Coefficient Limit in Potential Flow

The theoretical limit of lift coefficient is critical to provide the guidance for engineering design. This section gives the brief review of the study on the maximum limit coefficient for potential flows.

8.1 Flow Past a Circular Cylinder

Consider the inviscid flow around a circular cylinder where no separation occurs. The flow is synthesized by a uniform flow, a doublet and a vortex of strength Γ .

The velocity stream function for the flow is

$$\psi = V_{\infty} r \left(1 - \frac{R^2}{r^2}\right) \sin \theta + \frac{\Gamma}{2\pi} \ln \frac{r}{R} \quad (15)$$

The corresponding flow field is

$$V_r = V_{\infty} \left(1 - \frac{R^2}{r^2}\right) \cos \theta; \quad V_{\theta} = -V_{\infty} \left(1 + \frac{R^2}{r^2}\right) \sin \theta - \frac{\Gamma}{2\pi r} \quad (16)$$

The stagnation points can be obtained when $V_r = 0$ and $V_{\theta} = 0$. The resulting stagnation points depend on the value of $\Gamma/4\pi V_{\infty} R$. For $\Gamma/4\pi V_{\infty} R < 1$, both of the two stagnation points are located on the cylinder surface at (R, θ) , where θ is given by $\theta = \arcsin\left(-\frac{\Gamma}{4\pi V_{\infty} R}\right)$. If $\Gamma/4\pi V_{\infty} R = 1$, there is only one stagnation point on the bottom $(R, -\pi/2)$ on the cylinder surface. Larger circulation ($\Gamma/4\pi V_{\infty} R > 1$) moves the stagnation points off the surface [39, 40].

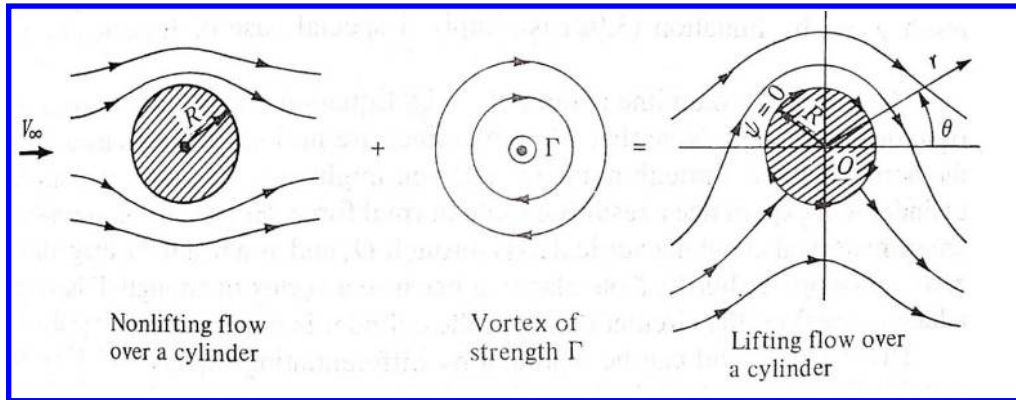


Figure 42: Superposition of flow over a cylinder.(Plot adopted from [39])

For the potential flow over a lifting circular cylinder, there are a infinite number of possible solutions, depending on the infinite number of Γ values.

8.2 Conformal Mapping

The conformal mapping is able to map any airfoil profile of a physical plane $p(x, z)$ onto a circular cylinder plane $P(X, Z)$, as shown in Fig. 43. The inverse transformation will therefore describe the exact solution of the

flow past the original profile. [40]

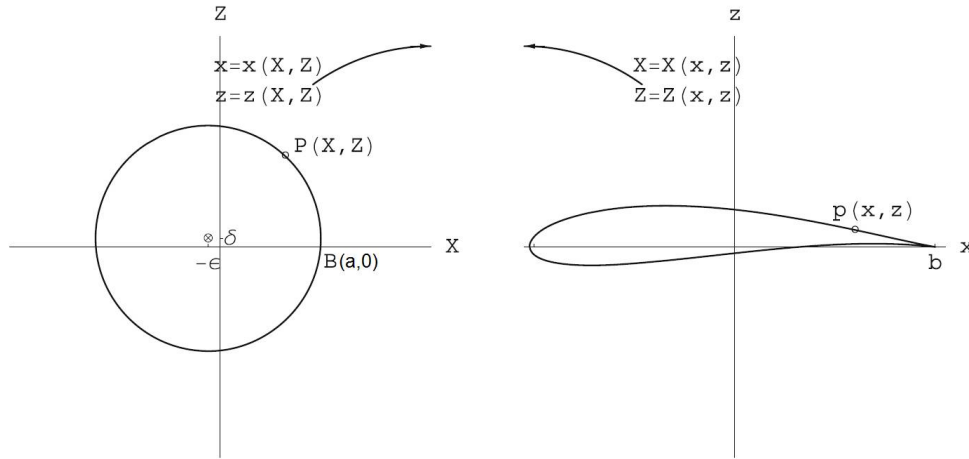


Figure 43: Conformal mapping from cylindrical plane (X, Z) to physical plane (x, z) . (Plot is from [40])

$$x = X \left(1 + \frac{a^2}{X^2 + Z^2} \right); \quad z = Z \left(1 - \frac{a^2}{X^2 + Z^2} \right) \quad (17)$$

where (x, z) represents the physical plane and (X, Z) represents the cylindrical plane. The cylinder of radius R , where $R^2 = (a + \epsilon)^2 + \delta^2$, centered at $X = -\epsilon, Z = \delta$ and passing through point $B(a, 0)$ maps onto a family of Joukowski airfoils depending on ϵ and δ . The profile has a cusp at the trailing edge, point b . [40]

8.3 The Kutta Condition

By the Joukowski transformation, the mapping of a cylinder to an airfoil profile is singular at $B(a, 0)$, which corresponds to the cusp at the trailing edge b of the Joukowski profile. For a realistic airfoil, the fluid particles is not able to come around the trailing edge, and hence separate from the profile there. This makes the inviscid flow solution unique by fixing the circulation Γ . The Kutta condition states that the flow must leave the airfoil at the sharp trailing edge smoothly. From the Joukowski transformation, for any flow with an incidence of α and an arbitrary circulation Γ around the cylinder, the rear stagnation point will be located at an arbitrary point. The velocity at the cusp of trailing edge is infinite. To enforce the Kutta condition, the circulation Γ is adapted to make the rear stagnation point located at the trailing edge. [40]

8.4 Flow Past an Ellipse Airfoil

The conformal mapping from an circle centered at the origin $(0, 0)$ and of radius $b(\geq a)$ in the cylindrical plane gives an ellipse airfoil.

The velocity potential with flow incidence of α , is

$$\Phi = V_{\infty} \left(r + \frac{b^2}{r} \right) \cos(\theta - \alpha) - \frac{\Gamma}{2\pi(\theta - \alpha)} \quad (18)$$

The velocity components on the cylindrical plane are,

$$V_r = 0, \quad V_{\theta} = -2V_{\infty} \sin(\theta - \alpha) - \frac{\Gamma}{2\pi b} \quad (19)$$

Using the Kutta condition, the circulation is obtained by $\Gamma = 4V_{\infty}b \sin \alpha$. Therefore, the lift coefficient is

$$C_L = \frac{2\Gamma}{V_{\infty}c} \quad (20)$$

Substituting the circulation,

$$C_L = 4\pi \frac{b^2}{b^2 + a^2} \sin \alpha = 2\pi \left(1 + \frac{t}{c} \right) \sin \alpha \quad (21)$$

where c is chord length, $c = 2(b^2 + a^2)/b$; t is the thickness, $t = 2(b^2 - a^2)/b$.

The maximum lift coefficient is achieved when the angle of attack reaches maximum $\alpha = 90^\circ$, which is $C_{L_{max}} = 2\pi \left(1 + \frac{t}{c} \right)$.

A.M.O.Smith (1975) [1] states that for any airfoil, the maximum possible lift is 4π for the maximum thickness is no greater than 1. Maximum circulation and thus lift coefficient is obtained when the two stagnation points coincide. Also the Kutta condition sets the circulation to such strength that the rear stagnation point is already at the trailing edge. It is called a natural flow [1]. For the ellipses family with no sharp trailing edge, the circulation may not be at the trailing edge. Thwaites [1] proposed the airfoil by suction to force the rear stagnation point to the rear end. Following the thought, greater circulation moves the stagnation point off the body. For instance, a Flettner Rotor generates such flows that move the stagnation off the body. However, it is considered as not realistic analog for a natural aerodynamic airfoil without flow control, where both of two stagnation points are on the surface. [1]

Therefore, it can be generalized that, for a airfoil with certain thickness t and rear stagnation point at the trailing edge, the maximum possible lift coefficient is obtained for potential flow over ellipse airfoils with Kutta condition at $\sin \alpha = 1$, which is

$$C_{L_{max}} = 2\pi \left(1 + \frac{t}{c} \right) \quad (22)$$

where $\frac{t}{c}$ represents the airfoil thickness. The maximum lift coefficient For a cylinder can be recovered from Eq. (22), which is 4π for an airfoil with $t/c = 1$ at $\alpha = 90^\circ$ It is a much higher value than what is typically obtained. The maximum lift coefficient of a single airfoil used in aircraft wings is typically about 1.5.